

NONEQUILIBRIUM RADIATION AND CHEMISTRY MODELS
FOR AEROCAPTURE VEHICLE FLOWFIELDS

aerospace
engineering
department



TEXAS A&M UNIVERSITY

Semiannual Progress Report
June 1989 -- December 1989

TAMRF Report No. 6382-90-01
January 1990

NASA Grant No. NAG-1-1003

Ireland A. C. C. C.

Professor of Aerospace Engineering

Texas A&M University

College Station, TX. 77843-3141

(NASA-CR-186379) NONEQUILIBRIUM RADIATION
AND CHEMISTRY MODELS FOR AEROCAPTURE VEHICLE
FLOWFIELDS Semiannual Progress Report, Jun.
- Dec. 1989 (Texas A&M Univ.) 50 pCSCL 01A

G3/02

Unclass
0269645

N90-28490

NONEQUILIBRIUM RADIATION AND CHEMISTRY MODELS
FOR AEROCAPTURE VEHICLE FLOWFIELDS

Semiannual Progress Report
June 1989 -- December 1989

TAMRF Report No. 6382-90-01
January 1990

NASA Grant No. NAG-1-1003

Leland A. Carlson
Professor of Aerospace Engineering
Texas A&M University
College Station, TX 77843-3141

NONEQUILIBRIUM RADIATION AND CHEMISTRY MODELS FOR AEROCAPTURE VEHICLE FLOWFIELDS

I. Introduction

This reports covers approximately the period June 1989 thru December 1989. The primary tasks during this period have been the initiation of the project, the continued development and improvement of the viscous shock layer nonequilibrium chemistry blunt body engineering code, the incorporation in a coupled manner of radiation models into the VSL code, and the initial development of appropriate precursor models. As a general statement concerning progress during the last six months, it should be noted that like all new projects the present one has been slow in starting. In addition, the move to our new building coupled with finals week and holidays did hinder research during the latter part of November and during December. Nevertheless, it is believed that while progress has been somewhat slower than desired, it has been steady and several initial milestones have been achieved.

II. Personnel

The staff associated with this project during the present reporting period have been Dr. Leland A. Carlson, Principal Investigator, and Thomas A. Gally and Scott Stanley, Graduate Research Assistants. It should be noted that Mr. Gally is currently supported by a NASA Graduate Student Researchers Fellowship and will use the results of his research on this project in his PhD dissertation.. Mr. Stanley, who is supported entirely by this project, will use this results of his research for his masters thesis.

III. General Program Improvements

During the present reporting period several general changes have been incorporated into the nonequilibrium chemistry viscous shock layer engineering code. Most of these have dealt with thermal nonequilibrium and chemical nonequilibrium effects. In particular, the shock jump conditions have been modified to properly include the fact that T_e is unequal to T_h immediately behind the shock front; and the static enthalpy and specific heat computations, which previously were computed using curve fits, have been replaced with partition function expressions that properly include thermal nonequilibrium. Further, the total energy equation has been changed so as to more correctly include thermal nonequilibrium effects, which has resulted in an improvement in the conservation of total enthalpy.

In addition, work has progressed on deriving an appropriate viscous shock layer full free electron energy equation. Currently, the program utilizes a quasi-equilibrium free electron energy equation; and it is planned to eventually replace this approximate equation with a complete differential equation. However, the proper treatment of including diffusion and inelastic terms is still being studied as well as whether or not electronic-electron coupling needs to be explicitly included in the free electron equation.

Also under the classification of general improvements, the transport property calculations have been changed to utilize recently published expressions and curve fits. (Ref. 1). In addition, the original approach of handling reaction rates by inputting both the

forward and reverse rate for each reaction has been replaced by utilizing either a forward or reverse rate and obtaining the other from an equilibrium constant computed using partition functions. The latter approach leads to more correct equilibrium compositions, particularly with respect to the level of ionization, and is consistent with the present formulation of the nonequilibrium radiation correction factors.

Finally, the entire program has been converted to double precision arithmetic. This change invokes only a slight computational penalty and significantly improves the accuracy of the results.

IV. Radiation Coupling and Nonequilibrium Radiation Models

One of the primary objectives of this reporting period has been to incorporate the RADICAL (Ref. 2) radiation model into the viscous shock layer code and to do so in a manner which would include radiation gasdynamic coupling. To accomplish this task, all unnecessary portions of RADICAL, such as the equilibrium calculations, have been removed. In addition, first order corrections for local thermodynamic nonequilibrium effects (LTNE) for each of the atomic line and continuum radiation processes have been included. Currently, these LTNE corrections are those discussed in Ref. (3-5) and are limited to maximum values of one. Since the present forms only tend to exceed one in the thermal boundary layer near the wall and since in that region higher electronic states could be easily depopulated by collisional processes instead of radiative mechanisms, this approximation seems reasonable. Further, in the past inviscid computations (Ref. 6) have yielded reasonable estimates of radiative heating, indicating that very little radiation originates in the cool wall thermal layer.

While the inclusion of these initial LTNE factors has been straightforward, it should be noted that it has been a non-trivial task. In the radiation model, each individual atomic process included had to be identified and examined to ensure that it utilized the proper number density and was in a form compatible with the LTNE formulation. It is believed that this modification has been accomplished, with the possible exception being the free-free processes. Verification of the proper form for the latter is awaiting a translation of a Russian article.

It should be noted that while molecules can, at the option of the user, be included in the present radiation model, no LTNE factors have yet been included for molecular radiative processes. Since the formulation presented in Ref. (4) for molecules is very approximate, the appropriate form for the molecular LTNE factors is currently under investigation; and it is anticipated that they will be included during the next reporting period.

In addition to the LTNE modifications to RADICAL, the radiation model has been incorporated into the VSL code and radiation gasdynamic coupling included via a $\nabla \cdot q_r$ flux term in the overall energy equation. At the present time, a coupled solution is computed by first obtaining a converged solution that does not include radiation coupling. Then the radiation model is utilized to compute the radiation field and flux at each point, including emission and absorption. This radiation result is then utilized for typically ten viscous shock layer iterations before it is repeated. A typical stagnation line solution requires ten to fifteen radiation calculations with, as indicated, typically ten flowfield iterations in between.

On a Sun 3/50 workstation, which is a 20 MHz, approximately 3 Mips machine, the ten flowfield iterations require about 110 seconds while each radiation calculation requires about seven minutes. As can be seen, the radiation calculation dominates the problem; and studies are in progress to determine if the time required for these calculations can be reduced. Nevertheless, it is believed that these times are acceptable since on a mainframe machine such as a Cray Y-MP or IBM 3090 they would only require a few seconds.

Currently, the radiation coupled VSL code is in the process of debugging and evaluation. For these investigations, most cases being considered are limited to the stagnation line and, in order to keep the chemistry simple, the gas being considered is nitrogen. Since from a radiative standpoint, high temperature nitrogen is very similar to air, it is believed that this approach is reasonable for this point in the project.

V. Typical Results

In this section several results obtained using the nonequilibrium coupled radiation viscous shock layer model are presented. At this stage, these results should be considered preliminary since they are being primarily used to debug the code and models and to gain insight into the phenomena affecting the flowfield chemistry and radiation. In all cases, results are for the stagnation line, utilize fifty-one points between the shock and the wall, and the freestream is N_2 . The nonequilibrium chemistry model is the Case II Nitrogen Reaction System presented in Ref. 5, with the reverse rates being obtained via the equilibrium constants. In addition, the wall has been assumed to be a noncatalytic black body at 1650 deg K. This latter assumption has been used for convenience even though it is recognized that for many of the cases of interest that the heat transfer load will be more than adequate to induce ablation and to raise the wall temperature to values several thousand degrees higher.

AFE CFD Point 2

This condition corresponds to what is often referred to as the "max Q" computational point for one of the initial AFE trajectories at which the freestream velocity is 8.915 Km/sec, freestream pressure is 15.715 dyne/sq. cm. and temperature is 197.101 K. For this case, the nose radius has been assumed to be 2.3 meters, and both atoms and molecules have been included in the radiation calculations. Heating results are presented in Table I and the stagnation temperature and composition profiles are shown as Figure 1.

As can be seen, the results include electron thermal nonequilibrium but they assume vibrational equilibrium. Since for the AFE vibrational nonequilibrium effects will be significant and may affect the chemistry and the radiation, it is planned to include in the near future a vibrational nonequilibrium model in the nonequilibrium radiating VSL code. However, the present results assume $T_{vN2} = T$.

As shown on Figure 1, the electron temperature rapidly rises behind the shock front and equilibrates with the heavy particle temperature. However, as evidenced by the continual decrease in temperature and the variations in composition across the shock layer, the stagnation flow for this case is always in chemical nonequilibrium. Also, the wall thermal layer comprises approximately twenty percent of the 10.8 cm thick shock layer. It should be noted that the electron temperature and composition results shown on

Figure 1 are very similar to unpublished results previously obtained for this case using the inviscid AFETE code (Ref. 7) and an earlier version of the VSL code (Ref. 5).

As would be expected for this case, the radiation coupling effects for this case are very small and cannot be detected on plots comparing uncoupled and coupled solutions. However, as shown on Table I, there is a small amount of cooling, which can be observed by comparing corresponding cases such as uncoupled corrected with coupled corrected etc. Also, as mentioned above, the radiative heating results for this case include molecules without any LTNE factors; and thus they should be conservative with respect to the radiative heating estimates, which range from 4.76 to 7.21 watts/sq cm. Note that the usage of the atomic LTNE corrections factors only reduces the radiative heating about 0.7 watts/sq cm, indicating that most of the radiation is probably molecular.

Since results have been obtained for this case previously using different versions of the method, the sensitivity of the results to various factors can be observed. For example, with the VSL code version, forward and reverse rate reaction chemistry, and the eight step radiation model used in Ref. (5), the non-radiation coupled results were with no LTNE corrections 29.7 watts/sq cm and 22.4 watts/sq cm with atomic LTNE corrections only. For these cases the electron temperature profile in the nonequilibrium zone was slightly higher than those shown on Figure 1 due to the influence of different reaction rates. On the other hand, after the shock jump and enthalpy changes involving electron temperature were incorporated but before the forward and reverse rates were replaced with the forward rate and an equilibrium constant, the results for columns (3) and (4) of Table I were, using RADICAL, 15.9 and 12.6 watts/sq cm respectively. Thus, radiative heating results are sensitive to small details in the methods, the radiation model, and in particular to the chemistry and electron temperature. It should be noted that the change from forward and reverse rates to only a forward rate and a computed equilibrium constant significantly changed the equilibrium temperature and composition.

Since the results shown on Figure 1 and Table I for this case are in better agreement with the detailed inviscid results obtained using AFETE than previous VSL values and since they have been obtained using better models, they are probably reasonable estimates. However, the effects of vibrational nonequilibrium and chemical nonequilibrium on molecular radiation have yet to be included. Nevertheless, since the latter effects should most likely reduce radiative heating, the presents estimates may be conservative.

AFE CFD Point 4

It is believed that this condition corresponds to a "max Q" computational point for an AFE trajectory associated with a heavier vehicle at which the freestream velocity is 9.326 km/sec, freestream pressure is 26.4 dyne/sq. cm. and temperature is 200 K. For this case, the nose radius has also been assumed to be 2.3 meters, and both atoms and molecules have been included in the radiation calculations. Heating results are presented in Table I and the stagnation temperature and composition profiles are shown Figure 2, for which the shock layer thickness is 10.5 cm.

As can be seen, these results are very similar to those for the CFD Point 2 case, and the remarks concerning that case apply equally well here. In general, the predicted heating rates, which do not include molecular nonequilibrium radiation factors, are higher than those for CFD Two.

U = 14.5 km/sec, Altitude = 65 km

In a recent paper (Ref. 8) results have been presented for the stagnation line of a one meter nose radius body at a trajectory point possibly representative of an earth entry return from Mars. These results include chemical nonequilibrium, thermal nonequilibrium assuming that the N_2 vibrational temperature and electron temperature are equal, and uncoupled nonequilibrium radiation computed by a detailed model that includes the molecular continuum and atomic lines. However, it is unclear whether or not the latter includes atomic continuum radiative processes (free-bound).

Using this model, the investigators obtained for this trajectory point an uncoupled radiative heating rate of 1700 watts/sq cm, a shock standoff distance of 5.7 cm, and a post-shock chemical nonequilibrium zone 1.1 cm thick. In this nonequilibrium zone, the electron-vibrational temperature never significantly exceed the equilibrium temperature. They also claimed that most of the radiative heating was from the ultra-violet below 2000 Å, that it originated from the nonequilibrium region behind the shock wave, and that very little was absorbed in the wall thermal layer. The latter is different from previous beliefs by some researchers (Ref. 9), but it is in agreement with the approximate studies of Carlson (Ref. 3).

In addition, in Ref. 8 comparisons were made with results obtained using the RASLE code (Ref. 10), which is an equilibrium viscous shock layer code using a radiation model also based upon RADICAL. Using the RASLE code, Ref. 8 obtained for the same case a shock standoff distance of 3.5 cm and a radiative heating rate of 970 watts/sq cm. The authors attributed the differences to nonequilibrium chemistry effects and the RASLE radiation model, asserting that the latter smeared atomic lines and therefore obtained incorrect results.

Considering these discrepancies, it is believed that it would be valuable to apply the model under development as part of this research to this trajectory point; and temperature and composition profile results for the case including radiative cooling are presented in Figure 3. For this case, the shock standoff distance is 3.4 cm; and, as can be seen, most of the shock layer is in chemical equilibrium.

The difference in shock standoff distance between the present results and those of Ref. 8 is believed to be primarily due to the electron temperature profile and its subsequent effect on chemistry. In Ref. 8, T_e is made equivalent to T_{vN_2} which keeps T_e low in the region behind the shock front. However, as shown in the composition profiles, diatomic species are insignificant over most of the shock layer and ionization dominates the chemistry. Thus, it would seem more appropriate to use, as in the present model, a free electron temperature which is strongly influenced by collisional and ionization phenomena. Figure 3 shows that the result of using such an approach is an electron temperature which in the nonequilibrium zone behind the shock front significantly exceeds the shock layer equilibrium temperature. Since the dominant ionization mechanism behind the shock front is electron-atom collisions (Ref. 5) that are governed by the free electron temperature, this enhancement of T_e accelerates ionization, shortens the chemical nonequilibrium zone to about 0.4 cm, and decreases the overall shock layer thickness. It should be noted that this result shows the strong sensitivity of the overall solution to the electron temperature model at such trajectory points.

Radiative heating results obtained with the present model are shown on Table I. Since at these conditions the radiative transfer should be dominated by atomic processes and since for the predicted shock layer temperatures nitrogen should be a reasonable model for air (Ref. 11), these results, which have been obtained utilizing only atomic processes corrected for LTNE effects, should be appropriate. As can be seen, the predicted stagnation point radiative heat transfer for the case without any radiation gasdynamic coupling is 1691 watts/sq cm, which is in remarkable agreement with the corresponding prediction of Ref. 8. It should be noted, however, that the present results indicate that most of the radiation originates from the high temperature equilibrium portion of the shock zone and not from the nonequilibrium part as postulated in Ref. 8. In the post-shock region, chemical nonequilibrium induces local thermodynamic nonequilibrium and depopulates the excited states rapidly via ionization, with the result that very little radiation originates in the nonequilibrium region.

Moreover, the radiation coupled results for this case indicate significant radiation cooling is present. This cooling is evidenced not only by the decrease in radiative heating to 1039 watts/sq cm but also by the temperature and ionization profiles on Figure 4. These figures compare the uncoupled and coupled results; and as shown by the steady decrease in temperature and in particular ionization throughout the equilibrium zone, radiation cooling for this case is significant and needs to be included in an analysis model.

As mentioned, the RASLE prediction for this case was 970 watts/sq cm. However, it is probable that the difference between this value and the present prediction is primarily due to the influence of reaction chemistry and the amount of absorption in the wall thermal layer. Since RASLE assumes equilibrium chemistry, it should predict more molecules in the wall layer and hence more absorption. This possibility is borne out by the fact that the RASLE results (Ref. 8) indicate that the wall thermal layer absorbs about 32% of the wall directed radiation while the present model indicates only about 15% is absorbed. Thus, it appears, that while most of the shock layer is in chemical equilibrium for this case, that chemical nonequilibrium effects may still be important and affect the radiative heating. In addition, it should be noted that the equilibrium chemistry formulation (i.e. forward and reverse rates or forward rate combined with equilibrium constant) strongly affects the heating results for this case. The results shown all used the forward rate combined with an equilibrium coefficient formulation.

It is mentioned above that Ref. 8 indirectly criticizes the RADICAL model, stating that it improperly handles line radiation by smearing the lines and that as a result it should give incorrect answers. Unfortunately, this assertion may be the result of a misinterpretation of the RADICAL radiation model and output. For convenience, RADICAL groups the radiative transfer into various wavelength regions and gives appropriate average values for these regions; and it is these values which are frequently plotted to show the variation of say wall radiative heating with wavelength or electron volts. An example of such a plot for the present case is shown on Figure 5, and at first glance it would appear that RADICAL does indeed smear lines to a significant extent. However, in the actual computation of the radiative transfer, RADICAL actually does for most line groups perform a line by line integration; and the final result is actually the consequence of such a detailed calculation.

When the results of the detailed RADICAL computation are plotted for the radiative flux to the stagnation point for this case, they appear as shown on Figure 6. Here a semi-log abscissa has been used in order to more vividly display the underlying continuum

radiation as well as the lines. As can be seen, there are strong lines in the infrared region below 4 ev and in the ultra-violet between 7 and 11 ev. However, in the vacuum ultra-violet above 11 ev many of the lines are actually absorbing part of the continuum flux as evidenced by the plots dropping below the continuum level. This absorption is also evident on Figure 7 where the stagnation heating is plotted versus wavelength. Here the line absorption of the continuum radiation is very evident around 0.1 microns as is the underlying continuum.

In general, the results shown on Figures 5-7 are very similar to Figures 3 and 4 in Ref. 8. However, careful comparison indicates that the present results have significant radiation above 11 ev primarily due to free-bound continuum processes, while those of Ref. 8 have little or no flux in this region. In Ref. 8 this difference is attributed to the usage of the smeared band line model in RADICAL; but, as shown on Figures 6 and 7, RADICAL does include the lines in detail in this region, and most of the radiation above 11 ev is due to the continuum, not the highly absorbing lines. This fact, combined with the absence of any significant radiation between 4 and 6 ev (.2 to .3 microns) in the results presented in Ref. 8, indicates that possibly Ref. 8 did not include atomic continuum radiation. Also, it is not clear whether or not Ref. 8 utilized for this case NEQAIR and accounted for LTNE effects. If it did not include LTNE effects it should predict higher values than the present method. On the other hand, if it also excluded atomic continuum phenomena, Ref. 8 would have missed some important radiative contributions and the two effects may have canceled. Thus, the seemingly good agreement between the methods may actually be serendipity.

Radiation Model Comparisons

Considering the possible sensitivity of various flowfield cases of interest to the radiative heating, it has been decided to compare several available radiation models and, if possible, evaluate the accuracy of RADICAL. For these comparisons, the following models have been used -- (1) RADICAL, (2) NEQAIR (Ref. 12), (3) and a modified 8-step band model based upon Ref. 13. Unfortunately, complete spectral comparisons have not been possible since in the available version of NEQAIR predictions below 2000 Å are unreliable. Further, NEQAIR does not automatically include absorption effects while RADICAL and the 8-Step model do. Thus, it has been decided to exclude the highly absorbing ultraviolet region and to limit the comparisons to the, by comparison, transparent visible and infrared region above 2000 Å. In addition, since LTNE factors are still under development, the comparison cases have assumed a constant temperature and pressure slab with the composition determined by the equilibrium calculation in RADICAL. For RADICAL and NEQAIR the gas has been considered to be air, while for the 8-Step model it has been considered equilibrium nitrogen at the same temperature and pressure. The results of the calculations are presented in Table II

As can be seen, the results of all three models are in very good agreement with the total variation in each case only being about 10 percent. This agreement is not really surprising since previous studies (Ref. 3-4) have shown that most models agree well in the visible and infrared. Thus, such comparisons and similar comparisons with experimental data in the visible and infrared are probably not very definitive. Nevertheless, considering that RADICAL agrees with other models and considering that it has been extensively compared to experimental data over a wide range of conditions (Ref. 2 and 6), it is believed that RADICAL is an excellent and adequate radiation model for the present research. In other words, the problems with predicting AOTV flowfields are not

associated with the primary radiation model. Instead the difficulties are a result of the sensitivity to chemistry, electron temperature modeling, LTNE factors, etc

Velocity Effects at 80 km

In order to assist in the debugging etc. of the model at this stage, results have been obtained for three different velocities, 12, 14, and 16 Km/sec, at an altitude of 80 Km. These velocities are, depending upon the trajectory chosen, within the possible range of entry velocities associated with a Martian return vehicle. In all cases, the results are for the stagnation line of a 2.3 meter nose radius vehicle, the freestream is nitrogen, and only atomic radiation is considered.

The temperature and composition profiles for the 12 km/sec case are shown on Figure 8, and the radiative heating rates are listed in Table I. As can be seen on the figure by the continually decreasing temperature and the variation in the N+ concentration, the entire shock layer at this flight condition is in chemical nonequilibrium. Immediately behind the shock front, which for the coupled case including LTNE factors is 10.7 cm from the wall, the electron temperature rises to a value several thousand degrees Kelvin above the expected equilibrium temperature and then gradually equilibrates with the heavy particle temperature. In the wall thermal layer, which comprises about 20% of the shock layer, deionization and recombination processes are important.

By comparing the uncoupled uncorrected radiative heating for this case with the uncorrected coupled result, it is apparent that for the uncorrected radiatively coupled situation, which assumes that electronic states are populated according to a Boltzman distribution, that there is significant radiation cooling. While not shown, comparison of uncorrected and corrected profiles indicates that this cooling occurs in the outer portion of the shock layer where the electron temperature is high. On the other hand, the corrected results, which include LTNE factors, shows only slight radiation coupling or cooling.

Results were also obtained earlier in this reporting period using a version of the code which utilized both forward and reverse rates instead of a forward rate and an equilibrium expression. In those cases, the level of ionization was about 50% higher and the temperature profiles, particularly in the region near the shock front were different in that the electron temperature was higher. As a consequence, the radiative heating rates comparable to those in Table I were a factor of two to three higher. This difference was primarily due to the higher electron temperature, and again demonstrates the sensitivity of radiative heating to composition and electron temperature.

Interestingly, the radiative heating value of 9.44 watts/sq cm predicted for the situation including radiation coupling and LTNE effects is remarkably close to the 10.5 watts/sq cm previously predicted for this case (Ref. 5). The latter was obtained using an earlier version of the model before the shock jump and chemistry improvements were incorporated. In addition, it used the 8-Step radiation model instead of RADICAL. However, the old shock jump conditions yielded a lower heavy particle temperature behind the shock front, which when combined with the older chemistry model predicted a very similar electron temperature profile. As a consequence, the heating rates were similar. Again, the sensitivity of radiative heating to electron temperature is evident.

The temperature and composition profiles for the 14 km/sec case are shown on Figure 9, and the radiative heating rates are also listed in Table I. Since the freestream velocity is higher, the nonequilibrium zone behind the shock front is shorter than at 12 km/sec, occupying only the outer 50% of the 8.7 cm thick shock layer. Nevertheless, the flow is dominated by a nonequilibrium chemistry zone, composed primarily of N, N+, and e-, and the wall thermal layer. While N2+ peaks behind the shock front, it is very small over most of the shock layer. In addition, as can be seen in Table I, there is in the uncorrected case extensive radiative cooling. Examination of profiles for various cases indicates that for the uncorrected case that the cooling occurs primarily in the nonequilibrium region behind the shock front where the electron temperature is highest.

However, for the corrected cases the inclusion of LTNE nonequilibrium effects significantly decreases the radiation from the nonequilibrium portion of the shock layer since in those cases ionization processes deplete rapidly the excited atomic electronic states. As a result, while there is radiative cooling, what there is occurs in the equilibrium portion of the shock layer between Y/Y_{shock} of 0.2 and 0.6. In addition, the present results indicate that LTNE phenomena reduce the radiative heating by about 80% for this flight condition.

Finally, with respect the 14 km/sec case, it should be noted that the same trend exists as in the 12 km/sec case with respect to the sensitivity to the old and new reaction rate treatments. As before, the electron temperature is higher in the nonequilibrium zone with the old formulation; and the radiative heating is approximately a factor of two higher.

The temperature and composition profiles for the 16 km/sec case are shown on Figure 10, and the radiative heating rates are again listed in Table I. Here, the electron temperature immediately behind the shock front is very high, having a peak value in the corrected coupled case of slightly over 20,000 K, as is the amount of ionization, which is about 60%. Likewise, due to the increase in velocity, the nonequilibrium zone is somewhat shorter. In this case it is about 30-40% of the 7.32 cm shock layer.

As would be expected, the radiative heat transfer results have the same trend as those for 14 km/sec. The uncorrected cases exhibit significant radiation coupling and cooling, with almost all of the cooling occurring from the nonequilibrium portion of the shock layer thru the shock front due to the very high electron temperature in that zone. This type of behavior is consistent with that shown in Ref. 3 in that reference's study of the sensitivity of the flowfield to radiation parameters. On the other hand, when LTNE effects are included (corrected results), the radiative cooling is significantly less. As before, it occurs primarily in the equilibrium portion of the shock zone.

Finally, for all three flight velocities, the predicted radiative heating is significant compared to the convective heating; and, in the 16 km/sec case, the radiative heating exceeds the convective prediction by 70%. While the latter is only approximate in that only 51 points have been used in these calculations and that the wall has been assumed fully noncatalytic, it is probably reasonably accurate. Also, since it is anticipated that advanced heat shield materials can withstand only up to 70 watts/sq cm without ablating, these results indicate that at 80 km ablative heat shields would be required on 2.3 meter nose radius vehicles at velocities of 14 km/sec and above.

U = 16 Km/sec Altitude = 75 Km and 72 Km

In order to investigate altitude effects and to determine the difficulty of using the model under a situation on a "large" vehicle where much of the shock layer is in equilibrium, results have been obtained for the 2.3 meter radius body at 16 Km/sec at 75 and 72 Km. The composition and thermal profiles for 75 Km are displayed on Figure 11, and in this case it can be seen that due to the lower altitude the chemical nonequilibrium zone is shorter occupying only about 15-20% of the shock layer. Likewise the entire shock layer is as a result of the higher pressure and density thinner than at 80 Km, having a thickness of 6.8 cm in the coupled corrected case.

Further, as shown on Table 1, even in the corrected case including LTNE effects there is significant radiative cooling. While difficult to detect on Figure 11, this cooling does affect the composition and temperature profiles in that the temperature is steadily decreasing in the "equilibrium" zone between 20 and 80%. Also, the degree of ionization actually peaks at Y/Y_{shock} of 0.85 and then due to cooling decreases by 50 percent before the effects of the wall thermal layer are encountered around $Y/Y_{\text{shock}} = 0.2$. Finally, it should be noted that for this case, the radiative heating dominates the problem and exceeds the convective rate by a factor of almost five.

The stagnation profiles at 72 Km are shown on Figure 12; and at this altitude the predicted shock layer thickness is 6.6 cm, only slightly smaller than the value at 75 Km. However, due to the increased pressure, the post-shock nonequilibrium chemical relaxation zone is considerably shorter at about 0.75 cm.; and the radiative heat transfer is approximately a factor of two larger at 758 watts/sq cm. Further, the temperature profile in the equilibrium zone is steadily decreasing; and the ionization level peaks at the end of the chemical relaxation zone and then decreases due to radiative cooling throughout the rest of the shock layer. This radiative coupling effect can be observed in the concentration profiles by noting the steady decrease in $[N^+]$ and increase in $[N]$ from the end of the nonequilibrium chemistry region at $Y/Y_{\text{shock}} 0.9$ to the beginning of the wall thermal layer around 0.15. Thus, for this case radiation coupling effects are important and do affect the temperature and composition of the shock layer.

Comparison with Inviscid Equilibrium Results

Even though a significant portion of any AOTV earth entry will be at altitudes where viscous and chemical nonequilibrium effects should be important, it is believed that it would be instructive to compare results obtained with the present model with inviscid equilibrium results. Such comparisons should indicate the validity of the present model and the limitations of equilibrium inviscid analysis predictions. As a result a limited number of cases have been computed in order to compare with the inviscid equilibrium tabular results of Sutton. The latter were obtained using a radiatively coupled solution of the inviscid flow equations at the stagnation point of a hemisphere and used RADICAL as the radiation model. This method has been compared extensively to ground test and flight measurements as described in Ref. 6. In comparing the Sutton values with the present results, it should be recognized that in addition to the inviscid-viscous and equilibrium-nonequilibrium differences, the Sutton results were obtained for air while the present values assumed a freestream of nitrogen and only include atomic radiation at this point.

In this comparison effort, four cases have arbitrarily been selected; and these are listed on Table III along with the inviscid equilibrium results. The corresponding viscous nonequilibrium heat transfer results are given in Table I, and the shock layer profiles are presented in Figures 12 - 15.

In general, the heating predictions from the two methods are of the same order of magnitude; and the shock standoff distances are similar. However, there are interesting differences. First, the shock standoff distances from the VSL nonequilibrium solutions are usually less than those obtained in the inviscid equilibrium cases. In the viscous nonequilibrium situation, the nonequilibrium zone behind the shock front has a lower than equilibrium density, which would tend to cause the shock layer to be thicker than in the equilibrium case. On the other hand, the wall thermal layer has a very high density due to the assumed cool wall temperature, which would cause the shock layer to be thinner. Apparently for the cases considered, the effects are counterbalancing with the result that the viscous nonequilibrium shock layer thickness is less than the inviscid equilibrium result.

The second interesting point is that in all cases the nonequilibrium viscous radiative heat transfer is less than the corresponding equilibrium inviscid value. In the nonequilibrium case, LTNE phenomena significantly reduces the radiation originating in the chemical nonequilibrium region behind the shock front and the cool temperatures in the wall thermal layer reduce radiation from that zone. Since the shock layer thicknesses are similar, these effects reduce the radiation heat transfer prediction to values below the equilibrium results.

In spite of the differences between the viscous nonequilibrium and inviscid predictions, it appears that the present results are reasonable and demonstrate the importance of including viscous, and chemical and radiative nonequilibrium effects in the AOTV flight regime.

VI. Comments on Method and Results

While the present viscous nonequilibrium model still needs significant development and improvement in many areas, it, even in its present form, offers several advantages over other existing techniques. First, it includes viscous and chemical nonequilibrium effects. Second, it is reasonably computationally efficient with respect to both time and resource requirements. Third, it utilizes a detailed radiation model, RADICAL, which accounts for the molecular continuum, atomic lines, and atomic continuum phenomena. Fourth, this model has been modified so that the effects of local thermodynamic nonequilibrium on the radiative transfer are included in the computation of the atomic radiation phenomena. Finally, fifth, the model includes multi-temperature effects in both the nonequilibrium chemistry and radiation models by computing via a free electron equation model an electron temperature. It is believed that this approach to the computation of radiation and chemistry effects is better than approaches which assume T_e equal to T_{vib} , particularly for those AOTV entries for which diatomic species are insignificant over most of the shock layer.

VII. Precursor Studies

A nonequilibrium phenomena of importance during high altitude aerocapture is the precursor effect, which involves the appearance of charged species, free electrons, and thermal nonequilibrium ahead of the shock front. This preshock ionization is believed to be primarily due to photoionization from the radiating shock layer, and it has been extensively studied for monoatomic gases and hydrogen atmospheres (Ref. 14-19). Since the presence of free electrons in front of the shock wave can lead to an enhanced free electron temperature which affects the post-shock electron temperature profiles, precursor effects should be included in nonequilibrium models in order to have the correct conditions behind the shock front. In addition, electron impact ionization reactions are governed by the electron temperature, and the nonequilibrium chemistry may be significantly affected by the pre-shock electron and electron temperature precursor. Finally, the change in electron temperature profiles might also affect the absorption and emission from the nonequilibrium region and the magnitude of radiative gasdynamic coupling.

Originally, it was believed that the effects of the preshock precursor could be easily included in the viscous nonequilibrium method by using the results of previous solutions, some of which are analytic, and modifying the freestream composition and conditions. However, a review of the literature revealed that very few studies considered air, that most previous studies did not simultaneously include all of the pertinent phenomena in analysing precursor effects, and that many utilized simplifying assumptions which might not be justifiable in the AOTV flight regime. For example, some assumed constant pressure while others showed that the pressure wasn't constant (Ref. 16 and 19). Likewise, many investigators ignored collisional chemistry in the precursor region while Foley and Clarke (Ref. 15) found it to be important in the near precursor in argon. Similarly, some ignored radiative gasdynamic coupling and certain radiation phenomena in the shock layer; and many assumed thermal equilibrium throughout the precursor zone.

After considering these differing results, it has been decided that it would be desirable to develop a precursor model which in its final form would include for air simultaneously the effects of near field photoionization, far field photoionization, radiative gasdynamic coupling in the shock layer, collisional chemistry effects in the near precursor, and thermal nonequilibrium. While some previous investigators have concluded in many cases that precursor effects have a minor impact on post-shock phenomena, it is felt that such a model would still be valuable, particularly considering the lack of information concerning precursor phenomena at velocities and altitudes associated with AOTV entry. In any event, it should serve to delineate precursor effects and establish whether or not they have a significant impact on the vehicle flowfield and heat transfer.

Because the precursor problem is complicated involving many phenomena, it is being approached in a step by step fashion. Thus, the work and model developed to date is very preliminary, is only partially developed, and only includes some of the important phenomena. For example, the present model only considers the stagnation line, at this point only includes photodissociation and photoionization associated with continuum radiation that has not been corrected for local thermodynamic nonequilibrium phenomena, and assumes thermal equilibrium. Other phenomena such as collisional chemistry, line radiation absorption in the precursor, LTNE effects, and thermal nonequilibrium will be added later. Thus, the present results are preliminary, incomplete, and perhaps wrong; and they should be viewed only as being representative of the work in progress.

Governing Equations

Since the flowfield along the stagnation streamline in front of the shock wave is one dimensional, the governing equations are:

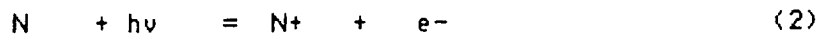
$$\text{Continuity: } \frac{\partial (\rho V)}{\partial n} = 0$$

$$\text{Momentum: } \rho V \frac{\partial V}{\partial n} + \frac{\partial p}{\partial n} = 0$$

$$\text{Energy: } \rho V \frac{\partial H}{\partial n} + \frac{\partial q_r}{\partial n} = 0$$

where H is the total enthalpy of the mixture and includes appropriate zero point energies. These equations can, of course, be integrated once to yield algebraic equations involving the unknowns ρ , V, p, and H in terms of the freestream quantities.

In addition to these equations, species continuity equations are needed in order to complete the problem. However, for the precursor problem, the exact form of these equations depends upon the reactions being considered in the precursor. At present, only the following photoprocess reactions are being considered:



where in each reaction $h\nu$ must be above an appropriate threshold level. Later, since it is expected that they are important in the near precursor immediately in front of the shock wave, collisional chemistry reactions will be added.

As discussed below, the individual species continuity equations can be written as

$$\frac{\partial c_i}{\partial n} = \frac{m_i}{\rho_\infty V_\infty} \int \frac{Y_i}{h\nu} \frac{\partial q_r \nu}{\partial n} d\nu$$

where the subscript i indicates species i. In this equation, Y_i is a factor which accounts for the proportion of the total radiation absorbed at frequency ν which causes a given photoreaction. Specifically,

$$Y_{N_2} = \frac{-K_{\nu_1}}{K_{\nu_{Tot}}} - \frac{K_{\nu_3}}{K_{\nu_{Tot}}} \quad Y_{N^+} = \frac{K_{\nu_2}}{K_{\nu_{Tot}}}$$

$$Y_N = \frac{2K_{\nu_1} - K_{\nu_2}}{K_{\nu_{Tot}}} \quad Y_{e^-} = \frac{K_{\nu_2} + K_{\nu_3}}{K_{\nu_{Tot}}} \quad Y_{N_2^+} = \frac{K_{\nu_3}}{K_{\nu_{Tot}}}$$

where K_{vj} is the absorption coefficient associated with photoreaction j and is zero below the energy threshold needed for that process to occur.

As can be seen, the individual species conservation equations require the evaluation of $\partial q_{rv} / \partial n$ prior to the integration over frequency. In the present approach, this term is obtained by numerically differentiating q_{rv} as computed by RADICAL, where effectively q_{rv} is

$$q_{rv} = 2\pi \int_{\gamma_v}^{\infty} S_v(t_v) E_2(t_v - \gamma_v) dt_v - 2\pi \int_0^{\gamma_v} S_v(t_v) E_2(\gamma_v - t_v) dt_v - 2\pi \int_{\gamma_s}^{\gamma_v} S_v(t_v) E_2(\gamma_v - t_v) dt_v$$

where γ_v is the optical thickness at the spatial location in the precursor under consideration. Notice that in the present model q_{rv} is evaluated using the flowfield in the shock layer as well as in the precursor and includes in detail the variations with frequency. This approach to precursor analysis is different than that of many previous investigators (Ref. 16 and 19 for example) who treated the shock layer as a boundary condition located at the shock front that radiated as some type of effective black body emitter. It is believed that the present approach not only is more accurate but also has the potential to permit coupled shock layer precursor solutions at a later date.

Rate of Production of Ions and Atoms

In the one dimensional flow before the shock front, the species continuity equation can be written

$$\frac{\partial \rho_i}{\partial t} + \frac{\partial (\rho_i u)}{\partial n} = \dot{w}_i$$

where w_i is the rate of production of species i and is given by

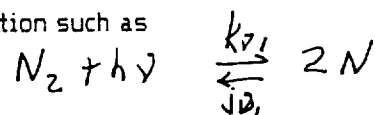
$$\dot{w}_i = \sum_{j=1}^r \dot{w}_{ij}$$

where the summation is over all the reactions being considered. For steady flow the species continuity equation can be expressed as

$$\rho_\infty u \frac{\partial c_i}{\partial n} = \dot{w}_i$$

where c_i is the mass fraction of species i .

Now each photoreaction such as



can be represented in the form

$$\sum_{j=1}^s a_{ij} X_i + h\nu \frac{k_{\nu j}}{j_{\nu j}} \sum_{j=1}^s a'_{ij} X_i$$

where a_{ij} and a'_{ij} are the stoichiometric coefficients for species j in reaction i , with the unprimed quantities being on the left hand side and the primed ones being on the right hand side. In addition, $k_{\nu j}$ and $j_{\nu j}$ represent the absorption and emission coefficients associated with each radiative process associated with the given reaction j . In the present analysis, each radiative process will be treated individually. Thus, a given frequency ν , may for some processes be above the threshold necessary to induce the photoreaction while for others it may be below. Thus, it will be convenient to introduce the absorption and emission coefficients, $k_{\nu r+1}$ and $j_{\nu r+1}$ which deal with absorption and emission which do not cause ionization or dissociation.

If for a given process and reaction it is assumed that every photon absorbed causes the photoprocess to occur, then the species production rate due to a given reaction process can easily be determined. For example for atomic nitrogen from reaction (1), the production rate of atomic nitrogen will be

$$\dot{W}_{N,1} = 2m_N \int_{\nu_{TH,1}}^{\infty} \frac{1}{h\nu} \int \rho_{N_2} (k_{\nu,1} I_{\nu} - j_{\nu,1}) d\Omega d\nu$$

while that for N_2 will be

$$\dot{W}_{N_2,1} = -m_{N_2} \int_{\nu_{TH,1}}^{\infty} \frac{1}{h\nu} \int \rho_{N_2} (k_{\nu,1} I_{\nu} - j_{\nu,1}) d\Omega d\nu$$

and similarly for the other reactions. Then by summing the production rate for each reaction

$$\dot{W}_i = \sum_{j=1}^r \dot{W}_{ij}$$

the total production rate for a given species can be determined. For example for atomic nitrogen, the result will be

$$\dot{W}_N = 2m_N \int_{\nu_{TH,1}}^{\infty} \frac{1}{h\nu} \int \rho_{N_2} (k_{\nu,1} I_{\nu} - j_{\nu,1}) d\Omega d\nu - m_N \int_{\nu_{TH,2}}^{\infty} \frac{1}{h\nu} \int \rho_N (k_{\nu,2} I_{\nu} - j_{\nu,2}) d\Omega d\nu$$

Under the quasi-equilibrium hypothesis, for each radiative process

$$\left(\frac{\partial I_\nu}{\partial n}\right)_j - \rho_i (k_{\nu j} I_\nu - j_{\nu j}) = k_{\nu j} (I_\nu - S_\nu)$$

where ρ_i is the absorbing species involved in the reaction. Thus,

$$\frac{\partial I_\nu}{\partial n} = \sum_{j=1}^{r+1} \left(\frac{\partial I_\nu}{\partial n}\right)_j = - \sum_{j=1}^{r+1} k_{\nu j} (I_\nu - S_\nu)$$

Then for a species such as atomic nitrogen the production rate can be expressed as

$$\dot{w}_N = m_N \int \frac{\partial Y_{\nu_1} - Y_{\nu_2}}{h\nu} \left[\int K_{\nu_{Tot}} (I_\nu - S_\nu) d\Omega \right] d\nu$$

$$Y_{\nu_1} = \frac{k_{\nu_1}}{K_{\nu_{Tot}}} \quad \text{and} \quad Y_{\nu_2} = \frac{k_{\nu_2}}{K_{\nu_{Tot}}}$$

where the Y_{ν_i} factors mentioned above have been introduced. However,

$$\int K_{\nu_{Tot}} (I_\nu - S_\nu) d\Omega = \left(\frac{\partial g_{R\nu}}{\partial n}\right)_{Tot}$$

which leads to the general species continuity equation for photoprocesses previously given, i.e.

$$\frac{\partial c_i}{\partial n} = \frac{m_i}{\rho_0 V_\nu} \int \frac{Y_i}{h\nu} \frac{\partial g_{R\nu}}{\partial n} d\nu$$

Absorption Coefficients

As can be seen in the general species continuity equation above, the accurate determination of species production due to photoprocesses depends upon the proper

representation of the appropriate absorption coefficients. In the present precursor model, absorption coefficients and radiation transport are computed using a modified version of RADICAL. In addition, since the present model is very preliminary only nitrogen continuum radiation is currently being included in the photoprocesses in the precursor. Line processes will be included in the next stage.

Originally, RADICAL included free-free ($h\nu > 0$ ev), low frequency ionization ($h\nu > 4.22$ ev), and high frequency photoionization ($h\nu > 10.8$ ev) processes for atomic nitrogen and the Birge-Hopfield ($6.5 < h\nu < 12.77$ ev) and 1st and 2nd Positive ($4.75 < h\nu < 4.5$ ev) bands for diatomic nitrogen. However, in order to make the model more applicable to the precursor region, several additions and modifications have been included in the manner in which it is used to compute the appropriate absorption coefficients for the species continuity equations.

Specifically, predissociation occurs in both the 1st and 2nd positive bands. Thus, an N_2 molecule in the A electronic state only needs to absorb a photon of 3.59 ev or greater in order to undergo predissociation via the $^5\Sigma_g^+$ state, while one in the B state only needs a photon of 4.6 ev or greater to dissociate by the $^3\Pi_u$ repulsive state; and these lower dissociation levels have been included as the threshold energies in the appropriate absorption coefficient (1st and 2nd positive) in the species continuity equations. However, since RADICAL only includes for 1st and 2nd positive energies up to 4.5 ev, the lower limit for predissociation from the B state has essentially no effect.

Initially, since it is well known that cool nitrogen has reasonably strong absorption in the ultraviolet, it was postulated that the Birge-Hopfield band should be extended above 12.77 ev with an essentially constant or slowly varying absorption coefficient value. However, calculations utilizing such an extension predicted dissociation levels in the precursor approaching ten percent and indicated extensive absorption of almost all the continuum radiation above 13 ev. Subsequent investigation and review of the literature has not verified the existence of Birge-Hopfield absorption in this region; and, thus, it is currently believed that any extension of Birge-Hopfield absorption above 12.77 ev is not justified.

Another band which might be important in the precursor is the Vergard-Kaplan band. Consequently, this band has been added to RADICAL; and an appropriate absorption coefficient relation developed based upon an f-number of $6.6E-07$ (Ref. 20). Based upon Lofthus (Ref. 21), this absorption coefficient should be applicable in the energy range 2.45 to 5.84 ev. However, since the photodissociation threshold for the VK band is 9.76 ev, it was originally postulated that the VK absorption coefficient should be extended above 5.84 ev, again assuming the coefficient to be slowly varying. However, subsequent investigations have revealed that the Vergard-Kaplan band both with and without the proposed extension has a negligible effect on the precursor phenomena. In addition, subsequent literature searches have failed to verify the existence of VK absorption at the higher energy levels. Consequently, for completeness Vergard-Kaplan absorption is currently included in the precursor model without any high energy extensions.

The Lyman-Birge-Hopfield absorption band is another band not originally included in RADICAL which might be important in precursor photodissociation. Like the 1st and 2nd positive bands, this band also exhibits predissociation at energies of 9.63 ev and above; and as a consequence, an absorption coefficient for this band has been developed for the range 4.77 to 8.5 ev based upon an f-number of $0.37E-05$ (Ref. 22). In addition, since

there is evidence that cool N_2 strongly absorbs in the LBH band at higher energies, the band has been extended from 8.5 eV to 12.4 eV assuming a constant absorption coefficient (Ref. 23).

The final change in the absorption coefficient model has been the inclusion of photoionization of N_2 to N_2^+ . Again, an appropriate absorption coefficient form has been developed following Ref. 24. However, the cross section has been adjusted to conform with the levels given by Ref. 23 and 25 for cool air.

Quite obviously, the present absorption coefficient model for the precursor region is very preliminary and subject to change; and the present investigators would welcome from NASA personnel any comments, suggestions, and additional information concerning these coefficients. Further literature searches and computational studies are in progress to determine the accuracy and adequacy of the present model.

Solution Scheme

At the present time the flowfield for the precursor region is obtained using an outer global and an inner local iteration scheme in order to solve the conservation equations and the radiation field in a coupled fashion. Initially, the flowfield in front of the shock wave is assumed to be the infinity conditions. Then the modified version of RADICAL is applied to both the shock layer and the precursor in order to obtain q_{total} , $\partial q_v / \partial N$, the K_v , and the Y_v at each point in the precursor.

The local flowfield values for this radiation field are then obtained at each point starting at the first unknown point furthest from the shock front. At the present time it is assumed that freestream values apply at the most upstream point. At each unknown point, continuity is used to determine density, velocity is obtained from momentum, total enthalpy from the energy equation, and static enthalpy from the total-static enthalpy relationship. Then the species continuity equations are integrated to obtain the species mass fractions from which temperature can be determined from the h - T relationship, and finally pressure can be obtained from the equation of state. This local or inner iterative process is then repeated until the flowfield values at that point do not change.

Once the solution is obtained at a point, the solution then progresses to the next point closer to the shock front; and this process is repeated until the entire precursor region has been obtained. At this point the entire global process is started once again by using RADICAL to obtain the radiation flowfield for the new precursor conditions. This global process involving both the radiation field and the flowfield is repeated until all the values in the precursor converge. At the present times, for the conditions so far considered, five global cycles are typically required for convergence.

Eventually, it is planned for this precursor process to also be coupled to the shock layer flowfield solution so that the entire flowfield can be obtained in a coupled fashion. However, the current preliminary precursor solutions have been obtained assuming that the shock layer flowfield properties are unaffected by the precursor.

Initial Results

As pointed out, the present model is very preliminary in that it only includes photoprocesses due to continuum radiation and assumes thermal equilibrium. In spite of these limitations, it is believed that test cases, even if somewhat unrealistic, will yield information concerning the phenomena involved and the influences of various parts of the model, as well as assisting in determining errors etc. in the model. Consequently, it has been decided to use as a test condition the shock layer at 12 km/sec for a 230 cm nose radius body at 80 km altitude. In addition, since the magnitude of the precursor effects depends directly upon the radiation intensity from the shock layer, the selected shock layer profiles correspond to those for the case without any radiation cooling and without inclusion of LTNE effects. In this manner, the precursor effects will be accentuated to values that, hopefully, will make them easier to perceive and understand. Consequently, the presented results should be viewed more from a trend and phenomena standpoint than from an actual value viewpoint.

Results corresponding to several different absorption coefficient models have been obtained for the test condition. These have included cases with and without the Birge-Hopfield extension, various N₂ single ionization absorption coefficients, cases with and without the Vergard-Kaplan extension, and various Lyman-Birge-Hopfield absorption coefficient forms. However, in order to avoid confusion, results are only presented for a single case; and the absorption coefficients used for for this case are shown on Figures 17-20 for a nominal temperature of 500 K. As can be seen, these particular coefficients do not include an extension to the Birge-Hopfield or the Vergard-Kaplan bands but do include one for the Lyman-Birge-Hopfield case. In addition, the N₂ single ionization absorption coefficient has a peak value similar to that recommended in Ref. 23 and 25.

The resulting temperature variation in the precursor for this case is portrayed on Figure 21, and there is a steady rise in the temperature as the shock front is approached. Since the present model still assumes thermal equilibrium, this temperature increase is relatively moderate. However, in the actual thermal nonequilibrium case, it would be expected that while the heavy particle temperature increase would be slightly less, the electron temperature rise would be significantly greater.

The variation of pressure and density in the precursor zone for the test case is shown on Figures 22 and 23. Notice that corresponding to the temperature increase there is a significant rise in pressure as the shock is approached, contrary to what has been assumed in many previous precursor analyses. On the other hand, the density variation and, thus, the velocity change is practically nonexistent.

Finally, the species concentrations in the precursor are plotted in Figure 24. Notice that for the absorption coefficients selected that there is measureable dissociation and atomic ionization. In addition, there is significant N₂⁺ ionization. Also, it should be noticed that these changes occur for the most part far away from the shock front; and, thus, the present continuum photoprocesses could be termed "far precursor" effects. It is anticipated that when atomic lines and collisional chemistry are included that these will have an influence in the precursor on the zone immediately in front of the shock and will determine the structure of what is termed the "near precursor". It is noted that the present far precursor type of solution produces a significant number of electrons, which should strongly influence atom-electron collisional chemistry in the near precursor.

VIII. Future Efforts

While it is difficult to anticipate what will be accomplished during the next reporting period, it is planned to continue the present studies and to initiate several new areas of investigation. In the general area of radiation gasdynamic coupling and nonequilibrium radiation models, the primary objectives will be to develop new formulations to account for local thermodynamic nonequilibrium effects associated with molecules and to improve the electron energy equation. In addition, it is planned to initiate efforts to include in the nonequilibrium viscous model excited atomic and molecular states as separate species. This approach, in which it is anticipated that the excited states of each species will be represented by a single approximate state, will require the introduction of "reactions" which control the populations of these states. In this manner second order improved formulations for LTNE effects will be included in the nonequilibrium problem.

Besides these efforts, it is hoped that in the next reporting period that an MCVDV type vibrational nonequilibrium model will be incorporated into the VSL nonequilibrium approach. Since vibrational nonequilibrium phenomena should be important at the lower velocity zone of the AOTV regime, this modification should greatly expand the usefulness of the present model. Further, since most wall type materials are catalytic to ion deionization but noncatalytic to atomic recombination, it is planned to modify appropriately the wall boundary condition to properly reflect this situation.

Of course, the eventual objective of the program is develop methods and codes which can be used to analyze the entire forebody of a vehicle entering the earth's atmosphere. Thus, work will probably be initiated during the next reporting period to extend the analysis to the entire forebody and to change the chemistry to be representative of air. (However, most model development will probably continue to consider only nitrogen since it is a good representation of high temperature air.) Finally, in developing the methods, consideration will always be given to the possible necessity of having to couple the flowfield solution to the precursor.

For the precursor studies, the primary objective during the next period will be to introduce thermal nonequilibrium into the problem by adding an appropriate electron energy equation. This equation will need to be more complex than the "quasi-steady" type of approach since it will have to include electron energy changes due to photoreactions as well as elastic and inelastic collisional phenomena. In addition, line emission absorption effects in the precursor will also be added to the model followed by collisional chemistry. Both of these items might be very important in the near precursor region immediately before the shock front. After these items are accomplished, consideration will be given to incorporating vibrational nonequilibrium into the precursor model; although, the necessity for this addition is not certain at this time. Finally, efforts will continue to improve the absorption coefficients applicable to the precursor region and to develop techniques for coupling the precursor solution to the shock layer solution.

In all of the efforts, particular attention will be devoted to detecting, noting, and investigating those parameters and phenomena which sensitively affect the flowfields and heat transfer rates, particularly radiative. In addition, attempts will be made to minimize CPU and computer resource requirements.

Finally, the original proposal anticipated that the entire effort would require approximately three or more years to complete. Consequently, a renewal proposal

outlining plans and budgets for the next year will submitted sometime during the next reporting period.

TABLE I -- Heat Transfer Results for Test Cases

Case			Radiative Heat Transfer				Convective Heat Transfer	
U _∞ (km/sec)	Altitude (km)	R _{nose} (m)	Uncoupled (watts/sq cm)		Coupled (watts/sq cm)		Comments	(watts/sq cm)
			Atomic LTNE Corrections					
			No	Yes	No	Yes		
8.915	77.9	2.3	7.21	6.05	5.46	4.76	Molecules Incl.	10.1
9.326	75.15	2.3	9.52	7.12	7.76	6.08	Molecules Incl.	16.0
14.5	65	1.0		1691		1039	Atomic Rad. Only	195
12	80	2.3	388	10.9	94.1	9.44	Atomic Rad. Only	30.5
14	80	2.3	1636	67.3	279	49.7	Atomic Rad. Only	49.8
16	80	2.3	4060	173	548	124	Atomic Rad. Only	70.0
16	75	2.3	3949	669	921	430	Atomic Rad. Only	89.9
16	72	2.3		1384		758	Atomic Rad. Only	103
16	72	1.0		738		518	Atomic Rad. Only	184
14	66	1.0		1004		657	Atomic Rad. Only	167
14	66	2.3		1815		971	Atomic Rad. Only	97.2

Table II --Wall Radiative Flux Above 2000 Angstroms

T_e (K)	Thickness (cm)	Pressure (atm)	Radical	Neqair	8-Step
(watts/ sq cm in all cases)					
12991	3.6	.3268	470	433	490
10844	12	.0264	18	17	19

Table III -- Inviscid Equilibrium Results from Sutton

Case U_{∞} (km/sec)	Altitude (km)	Nose Radius (m)	Radiative Heat Transfer (watts/sq cm)		Standoff Distance (cm)
			Adiabatic	Coupled	
16	72	2.3	2668	1066	7.75
16	72	1.0	1570	845	3.6
14	66	2.3	3208	1323	8.65
14	66	1.0	2054	1065	3.92

XI. Technical Monitor

The NASA technical monitor for this grant is Lin C. Hartung, Aerothermodynamics Branch, Space Systems Division, NASA Langley Research Center, Hampton, Virginia.

X. References

1. Gnoffo, P. A., Gupta, R. N., and Shinn, J., "Conservation Equations and Physical Models for Hypersonic Air Flows in Thermal and Chemical Nonequilibrium", NASA TAP 2867, February 1989.
2. Nicolet, W. E., "Advanced Methods for Calculating Radiation Transport in Ablation Product Contaminated Boundary Layers," NASA CR - 1656, September 1970.
3. Carlson, L. A., "Approximations for Hypervelocity Nonequilibrium Radiating, Reacting, and Conducting Stagnation Regions," J. of Thermophysics and Heat Transfer, Vol. 3, No. 4, October 1989, pp. 380-388.
4. Carlson, L. A., Bobskill, G. J., and Greendyke, R. B., "Comparison of Vibration Dissociation and Radiative Transfer Models for AOTV/AFE Flowfields," J. of Thermophysics and Heat Transfer, Vol. 4, No. 1, January 1990, pp. 16-26.
5. Carlson, L. A. and Gally, T. A., "The Effect of Electron Temperature and Impact Ionization on Martian Return AOTV Flowfields," AIAA Paper 89-1729, June 1989.
6. Sutton, K., "Radiation Revisted," AIAA Paper 84-1733, June 1984.
7. Carlson, L. A., "Computational Fluid Dynamics and Aerothermodynamics -- Final Report," Texas A&M Research Foundation Report No. 5671-89-01, March 1989.
8. Park, C. and Milos, F. S., "Computational Equations for Radiating and Ablating Shock Layers," AIAA Paper 90-0356.
9. Park, C., "Assesment of Two Temperature Kinetic Model for Ionizing Air," AIAA Paper No. 87-1574, June 1987.

10. Nicolet, W. E., Waterland, L. R., and Kendall, R. M., "Methods for Predicting Radiation Coupled Flowfields about Planetary Entry Probes," Aerodynamic Heating and Thermal Protections Systems, AIAA Progress in Astronautics and Aeronautics, Vol. 59, Ed. by L. S. Fletcher, AIAA, 1978, pp. 120-136.

11. Knott, P. R., Carlson, L. A., and Nerem, R. M., "A Further Note on Shock Tube Measurements of End Wall Radiative Heat Transfer in Air," AIAA Journal, Vol. 7, November 1969, pp. 2170-2172.

12. Park, C. "Nonequilibrium, Air Radiation (NEQAIR) Program: User's Manual," NASA TM B6707, July 1985.

13. Olstad, W. B., "Nongray Radiating Flow About Smooth Symmetric Bodies," AIAA Journal, Vol. 9, January 1971, pp. 122-130.

14. Nelson, H. F. and Goulard, R., "Structure of Shock Waves with Nonequilibrium Radiation and Ionization," Physics of Fluids, Vol. 12, Aug. 1969, pp. 1605-1617.

15. Foley, W. H. and Clarke, J. H., "Shock Waves Structured by Nonequilibrium Ionizing and Thermal Phenomena," Physics of Fluids, Vol. 16, March 1973, pp. 373-383.

16. Tiwari, S. N. and Szema, K. Y., "Effects of Precursor Heating on Radiative and Chemically Reacting Viscous Flow around a Jovian Entry Body," NASA CR 3186, October 1989.

17. Nelson, H. F., "Effect of a Finite Ionization Rate on the Radiative Heating of Outer Planet Atmospheric Entry Probes," NASA CR 3577, 1982.

18. Nelson, H. F., "Analytic Solution for Shock Wave Precursors," AIAA Journal, Vol. 13, Jan. 1975, pp. 115-117.

19. Tiwari, S. N. and Szema, K. Y., "Influence of Precursor Heating on Viscous Flow Around a Jovian Entry Body," NASA CR 3174, 1979.

20. Menard, W. A. and Thomas, G. M., "Experimental and Theoretical Study of Molecular, Continuum, and Line Radiation from Planetary Atmospheres," AIAA Journal, Vol. 6, April 1968, pp. 41-50.

21. Lofthus, A. "The Molecular Spectra of Nitrogen", Ph.D. Dissertation, University of Oslo, Blindern, Norway, Dec. 1960.

22. Allen, Richard A., "Spectrally Integrated Fluxes Including Line Contributions and Self Absorption," NASA CR-556, 1965.

23. Marr, G. J., Photoionization Processes in Gases, Academic Press, New York, 1967, pp. 176 and 236.

24. Zeldovich, Y. B. and Razier, Y. P., Physics of Shock Waves and High Temperature Hydrodynamic Phenomena, Academic Press, New York, 1966, pp. 279-271.

25. Zeldovich, Y. B. and Razier, Y. P., Physics of Shock Waves and High Temperature Hydrodynamic Phenomena, Academic Press, New York, 1966, pp. 605 ff.

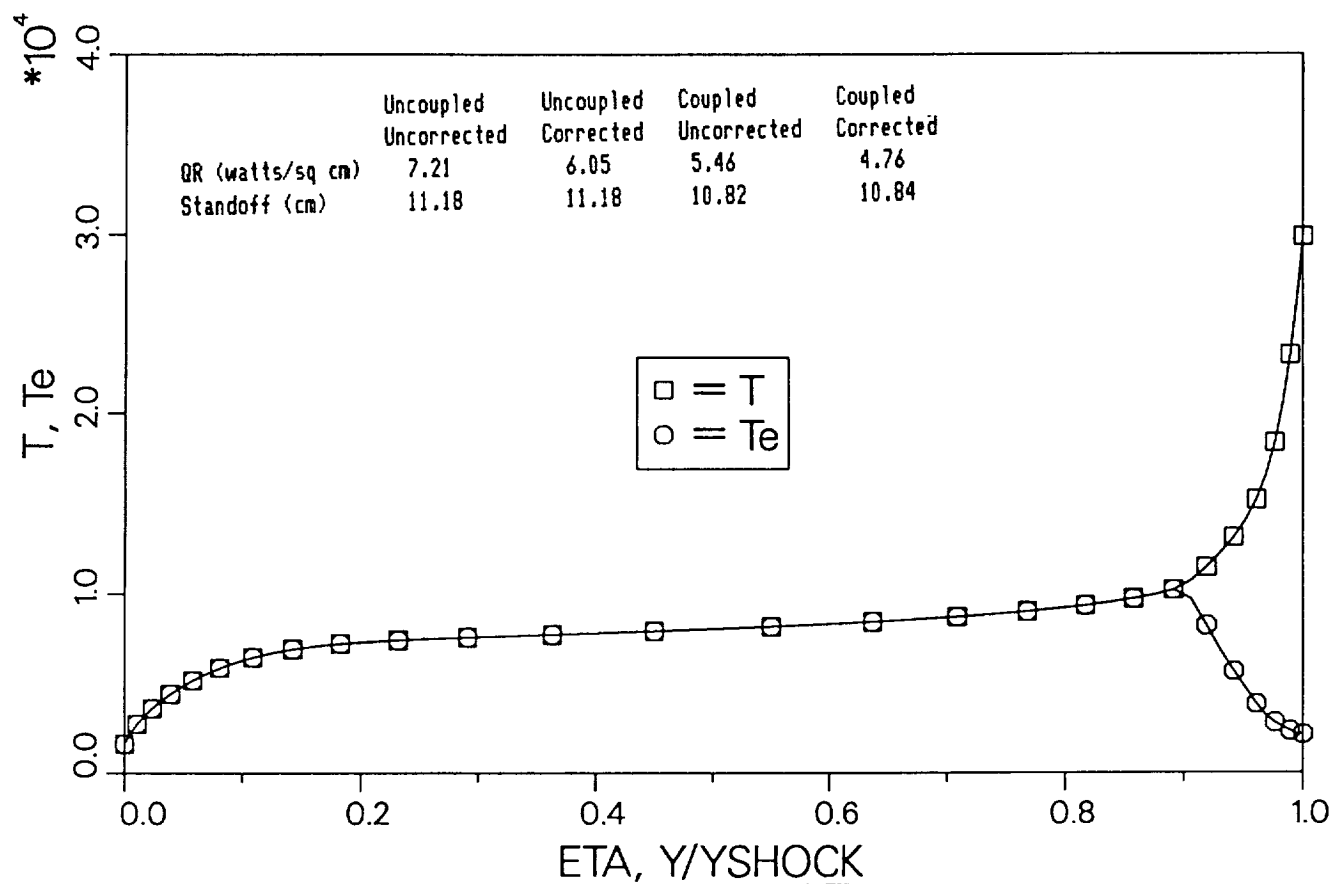
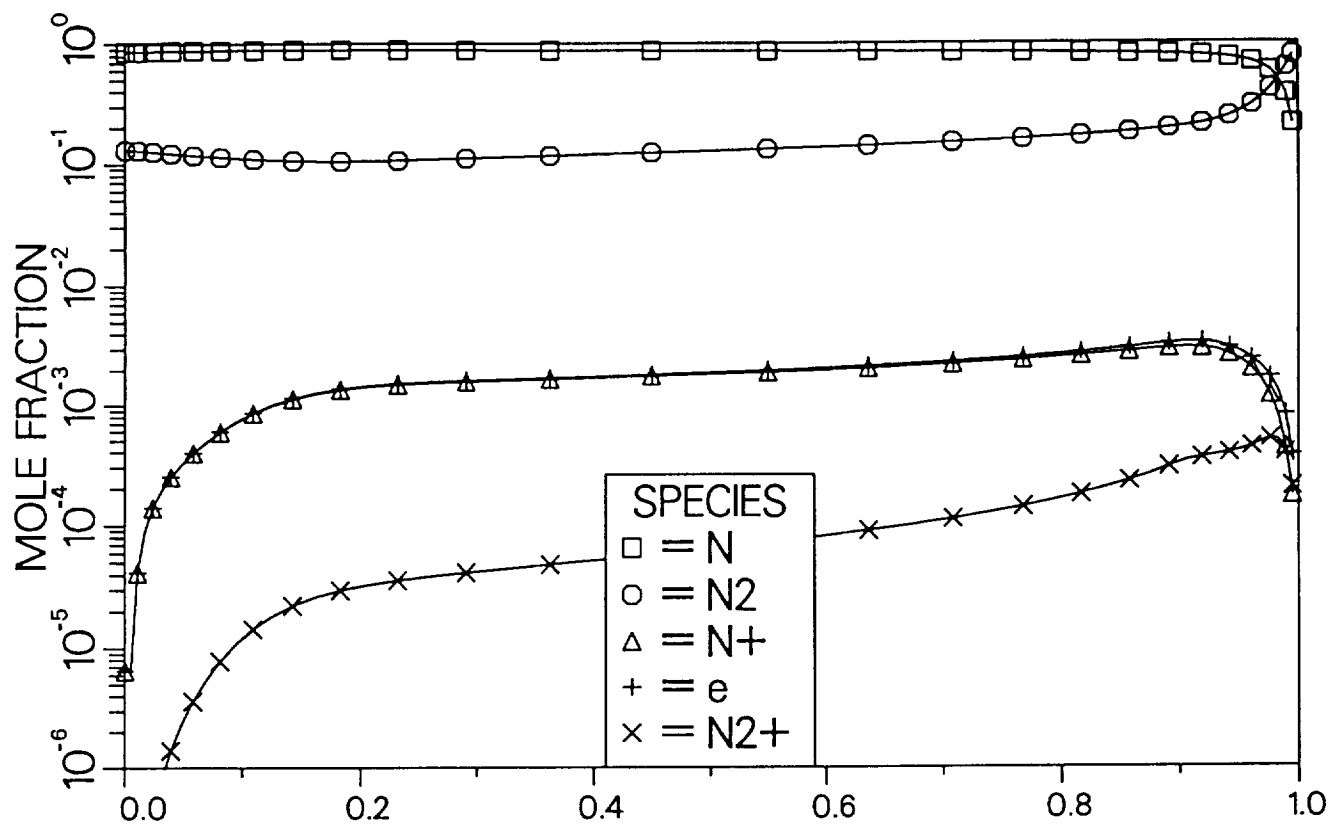


Fig. 1 -- Stagnation Profiles with Radiation Coupling and LTNE Effects
 $U = 8.915$ km/sec, $H = 77.9$ km, $R_{nose} = 2.3$ m
 $QR = 4.76$ watts/sq cm, $\delta = 10.84$ cm

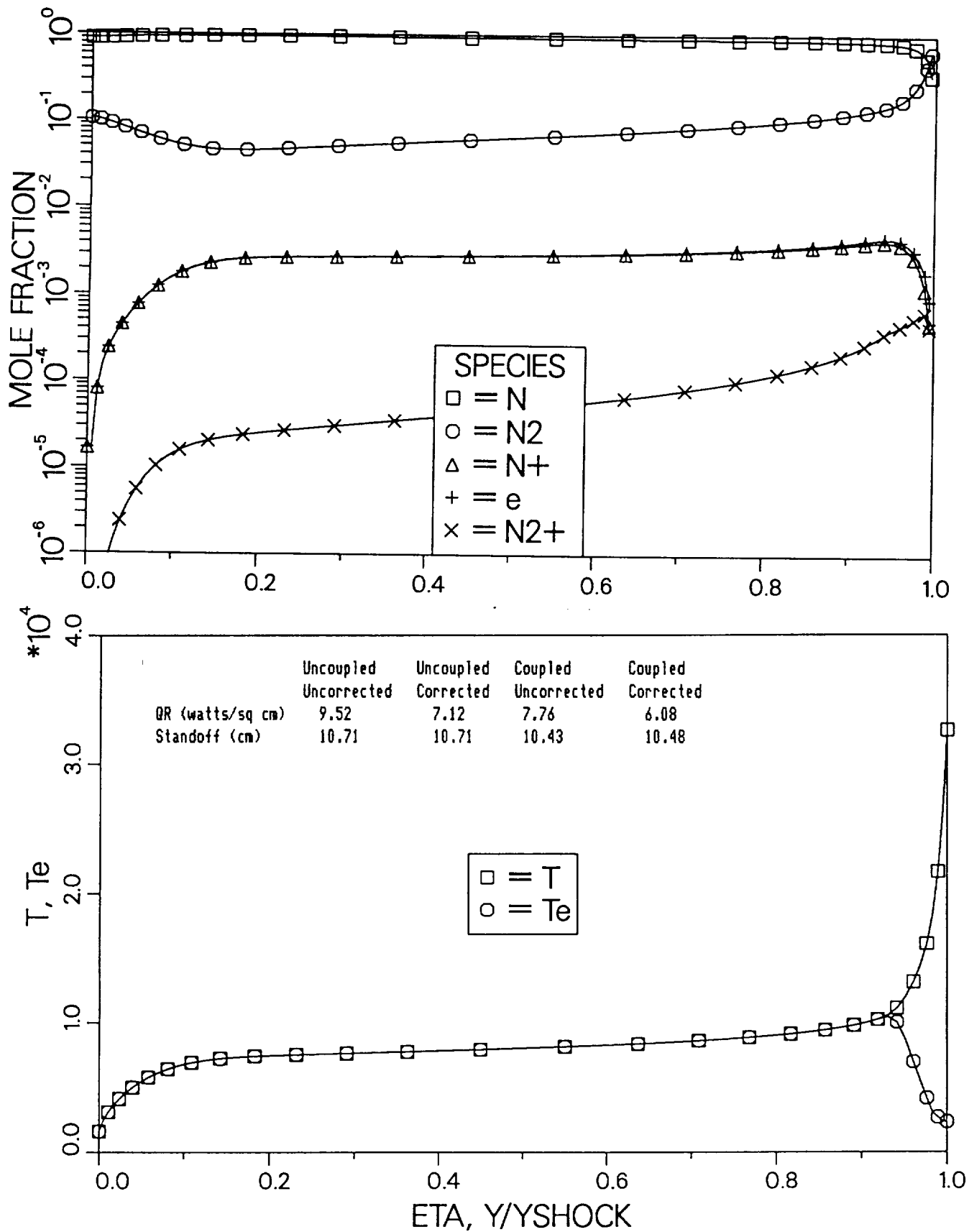


Fig. 2 -- Stagnation Profiles with Radiation Coupling and LTNE Effects
 $U = 9.326 \text{ km/sec}$, $H = 75.2 \text{ km}$, $R_{\text{nose}} = 2.3 \text{ m}$
 $QR = 6.08 \text{ watts/sq cm}$ $\delta = 10.48 \text{ cm}$

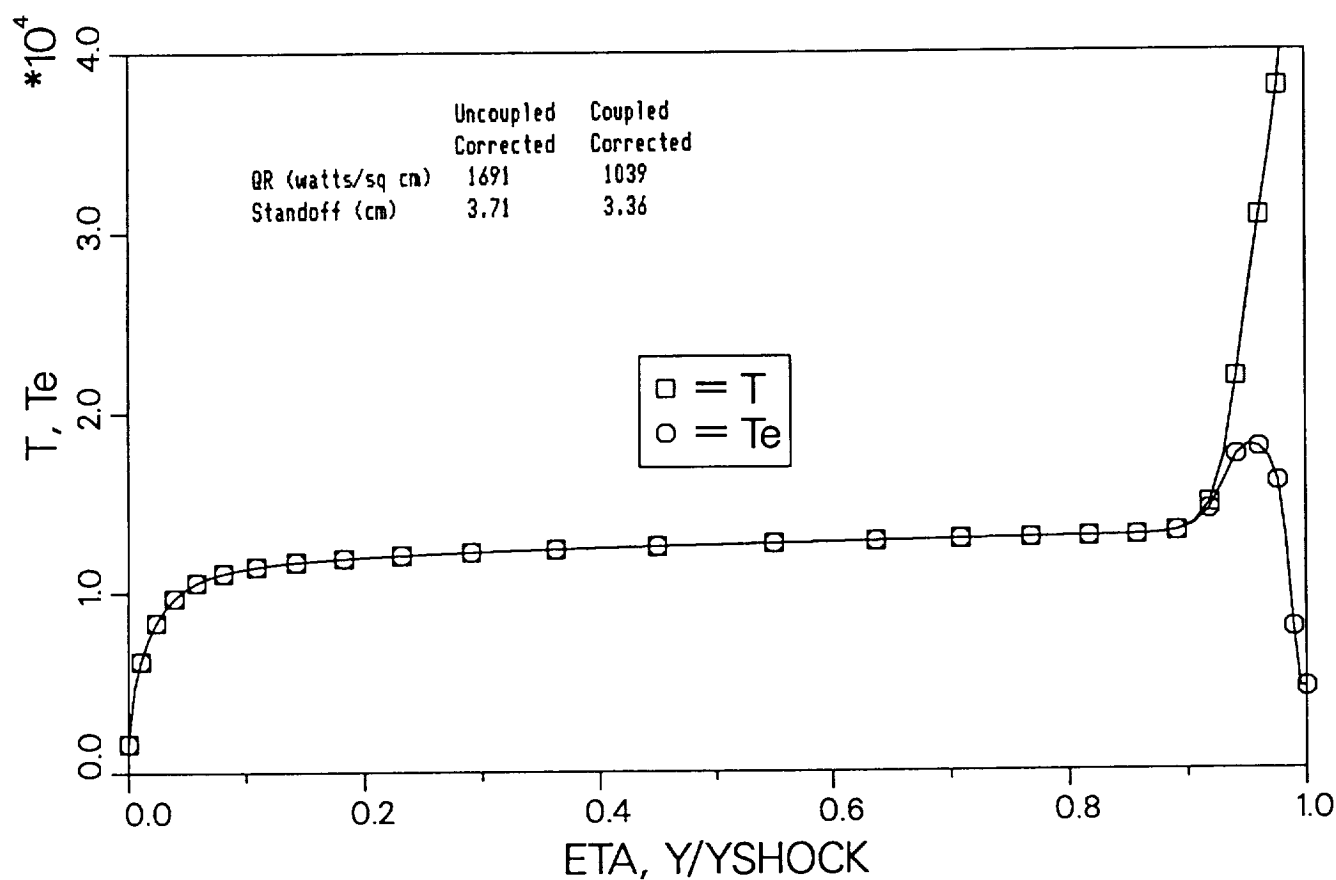
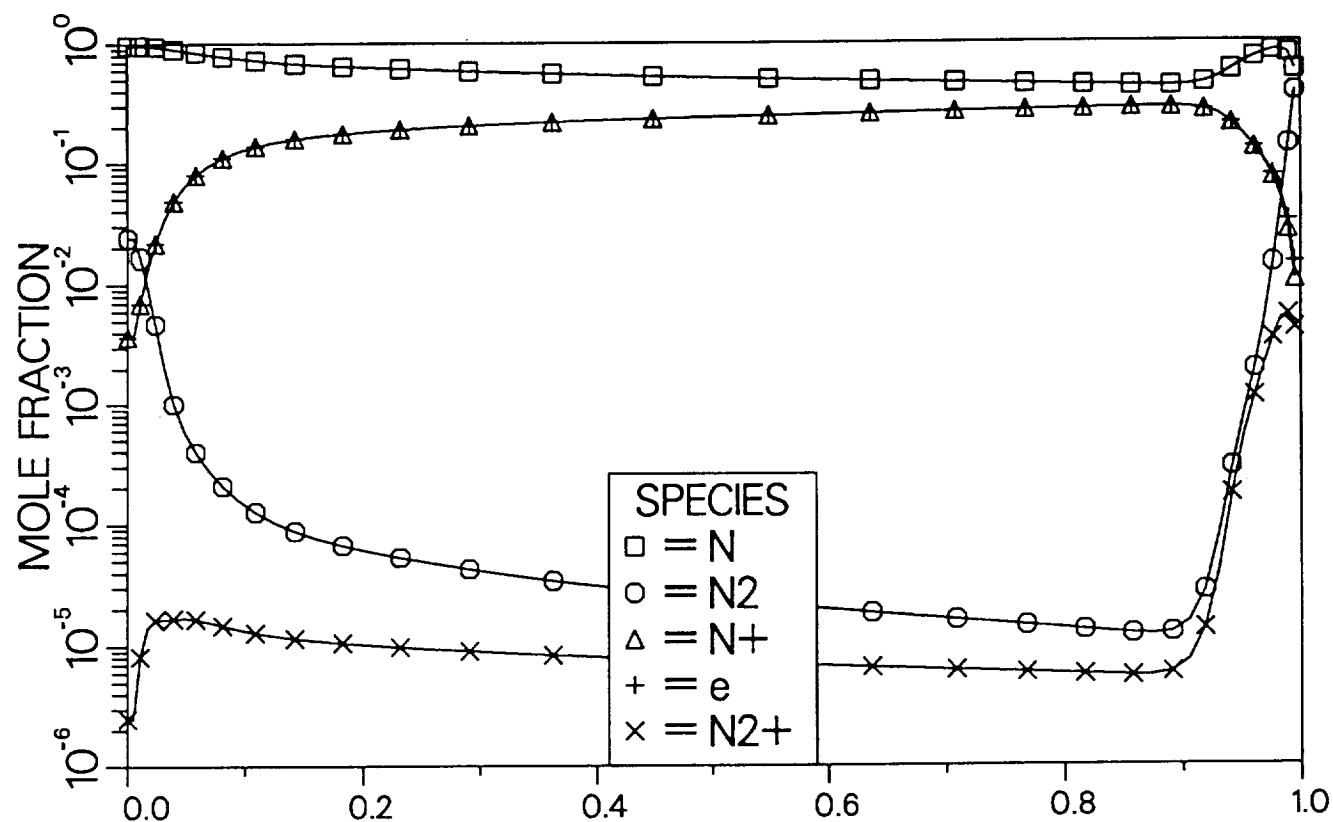


Fig. 3 -- Stagnation Profiles with Radiation Coupling and LTNE Effects
 U = 14.5 km/sec, H = 65 km, R_{nose} = 1 m
 QR = 1039 watts/sq cm ξ = 3.36 cm

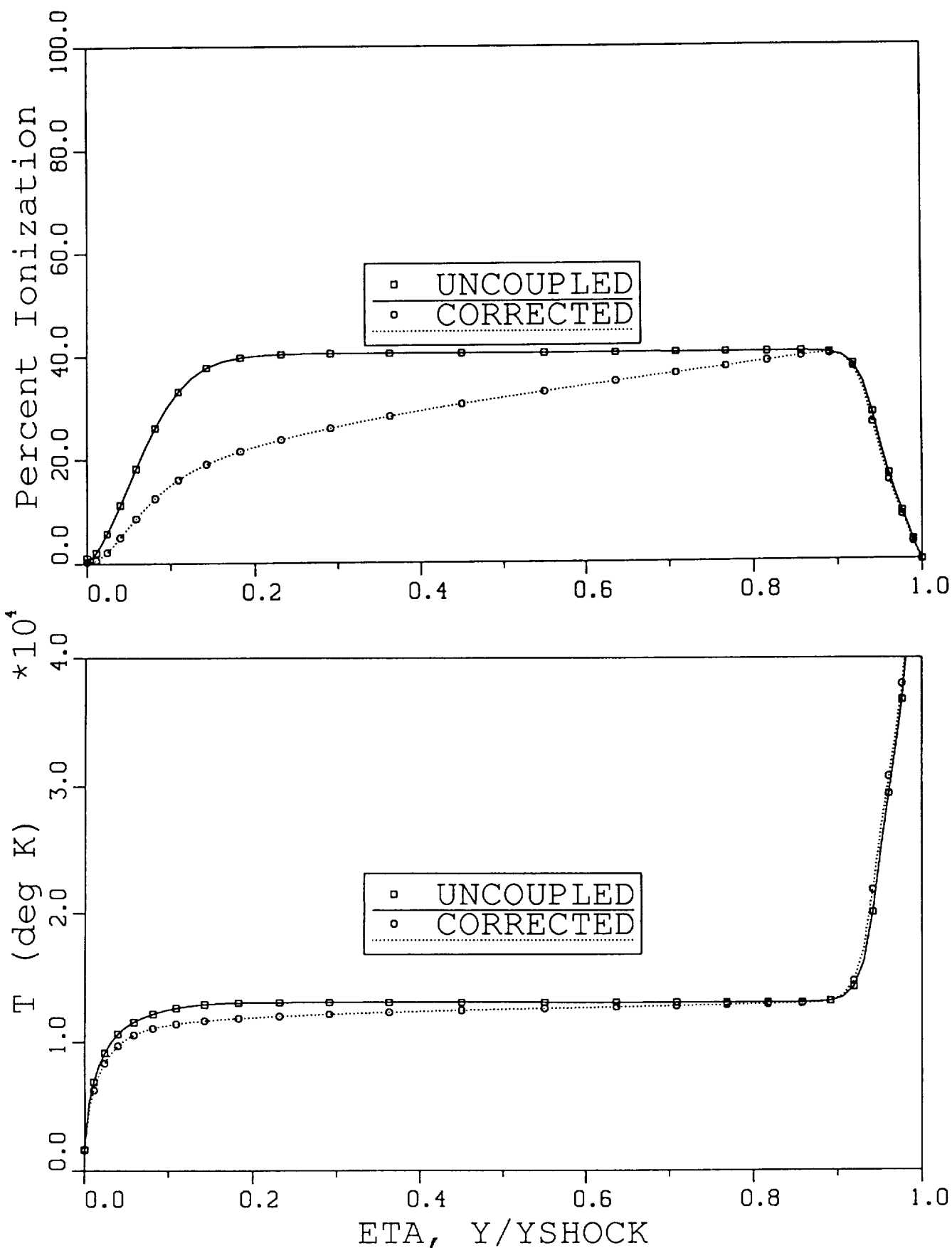


Fig. 4 -- Comparison of Uncoupled and Coupled Profiles. Both with LTNE Effects
 $U = 14.5$ km/sec, $H = 65$ km, $R_{nose} = 1$ m

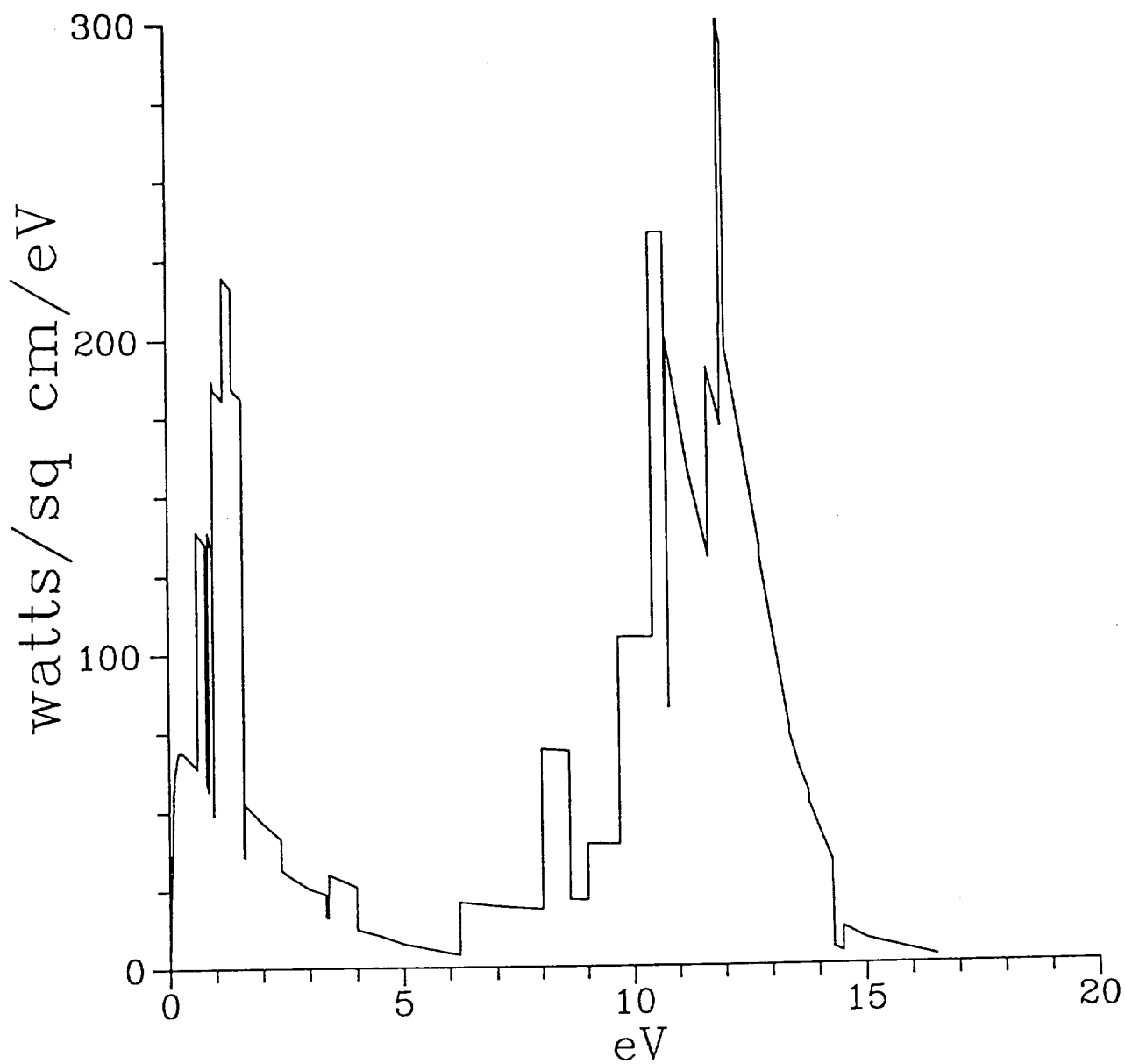


Fig. 5 -- Usual Presentation of Spectral Variation of Stagnation Point Heat Transfer
 $U = 14.5$ km/sec, $H = 65$ km, $R_{\text{nose}} = 1$ m

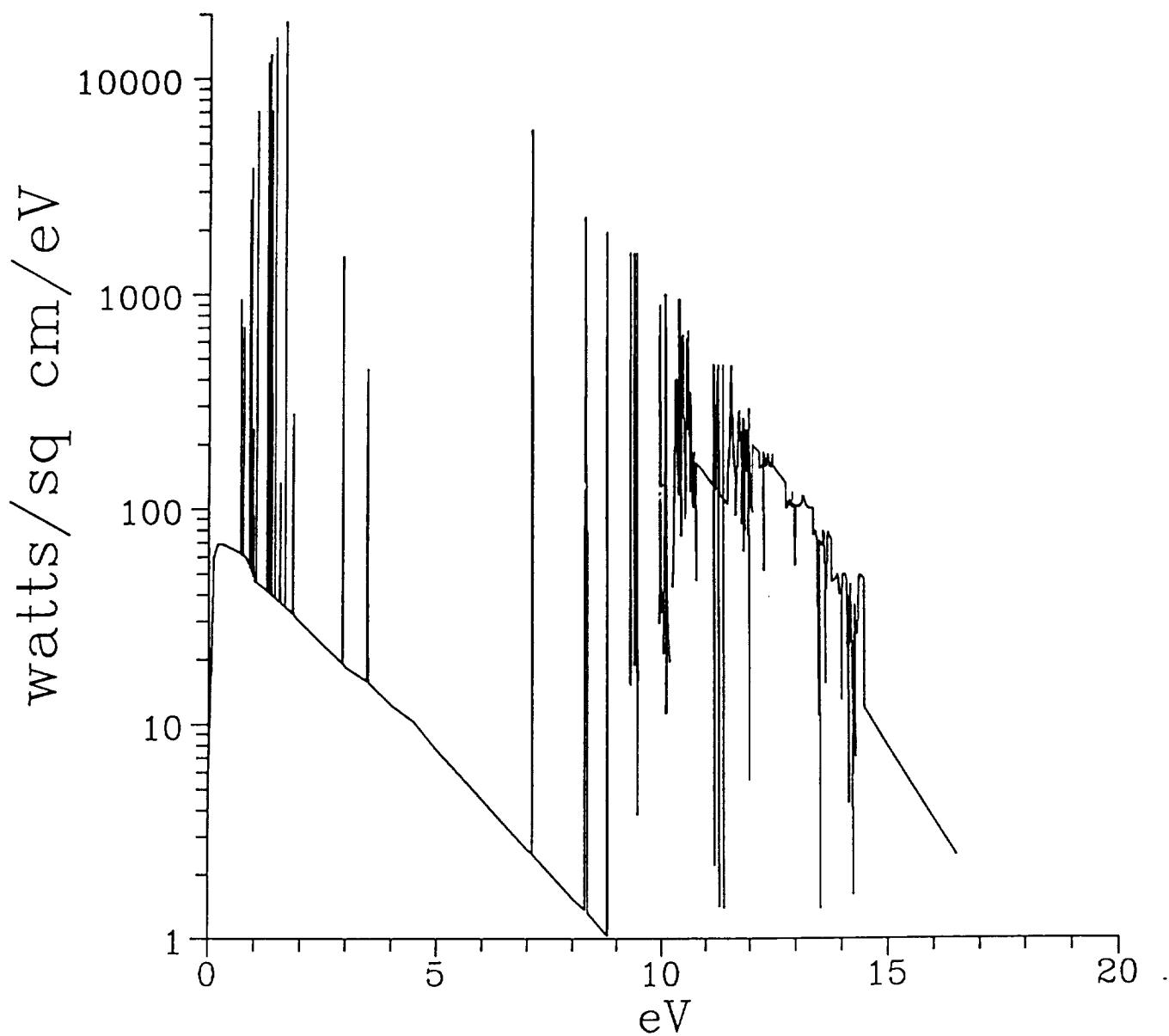


Fig. 6 -- Detailed Spectral Variation of Stagnation Point Heat Transfer
 $U = 14.5$ km/sec, $H = 65$ km, $R_{nose} = 1$ m

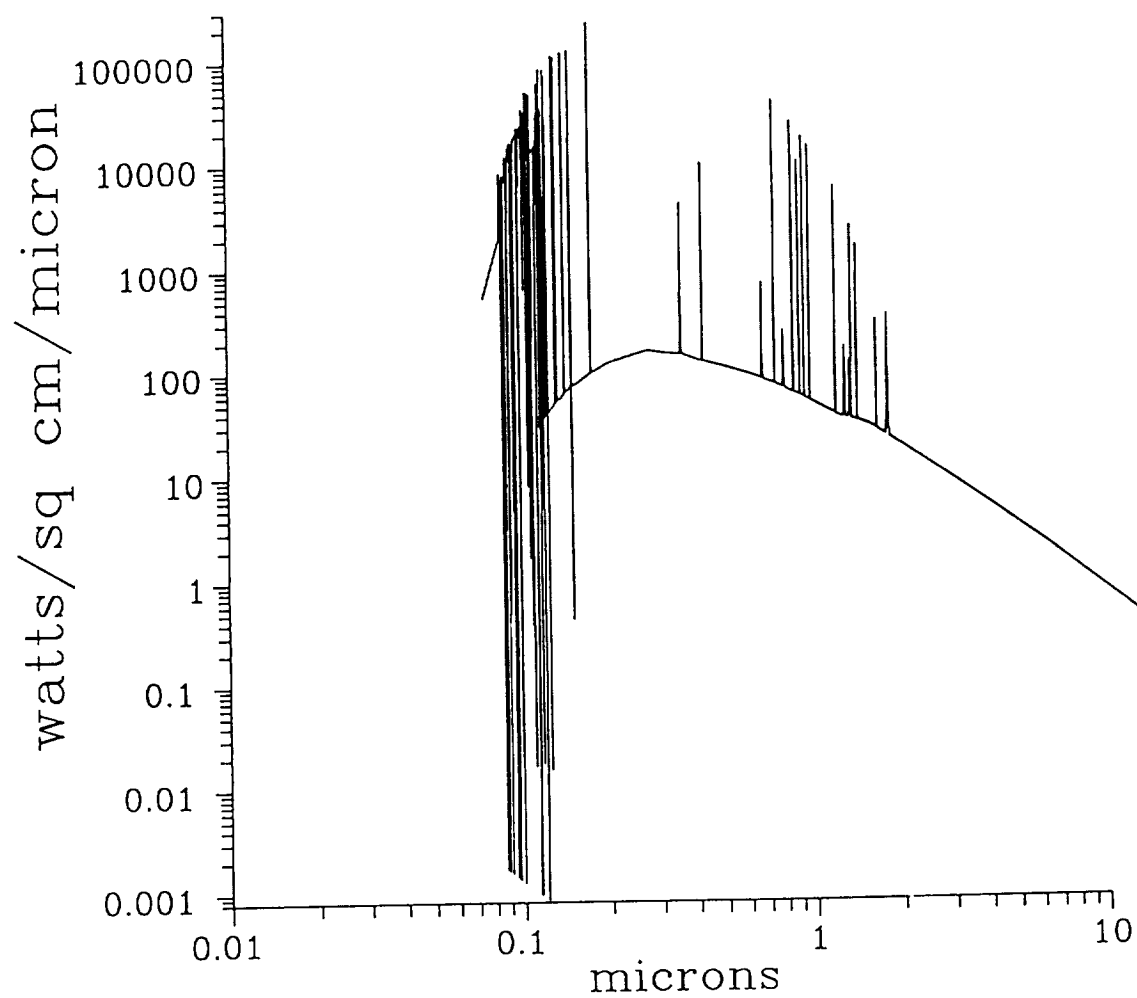


Fig. 7 -- Detail Spectral Variation of Stagnation Point Heat Transfer
 $U = 14.5$ km/sec, $H = 65$ km, $R_{nose} = 1$ m

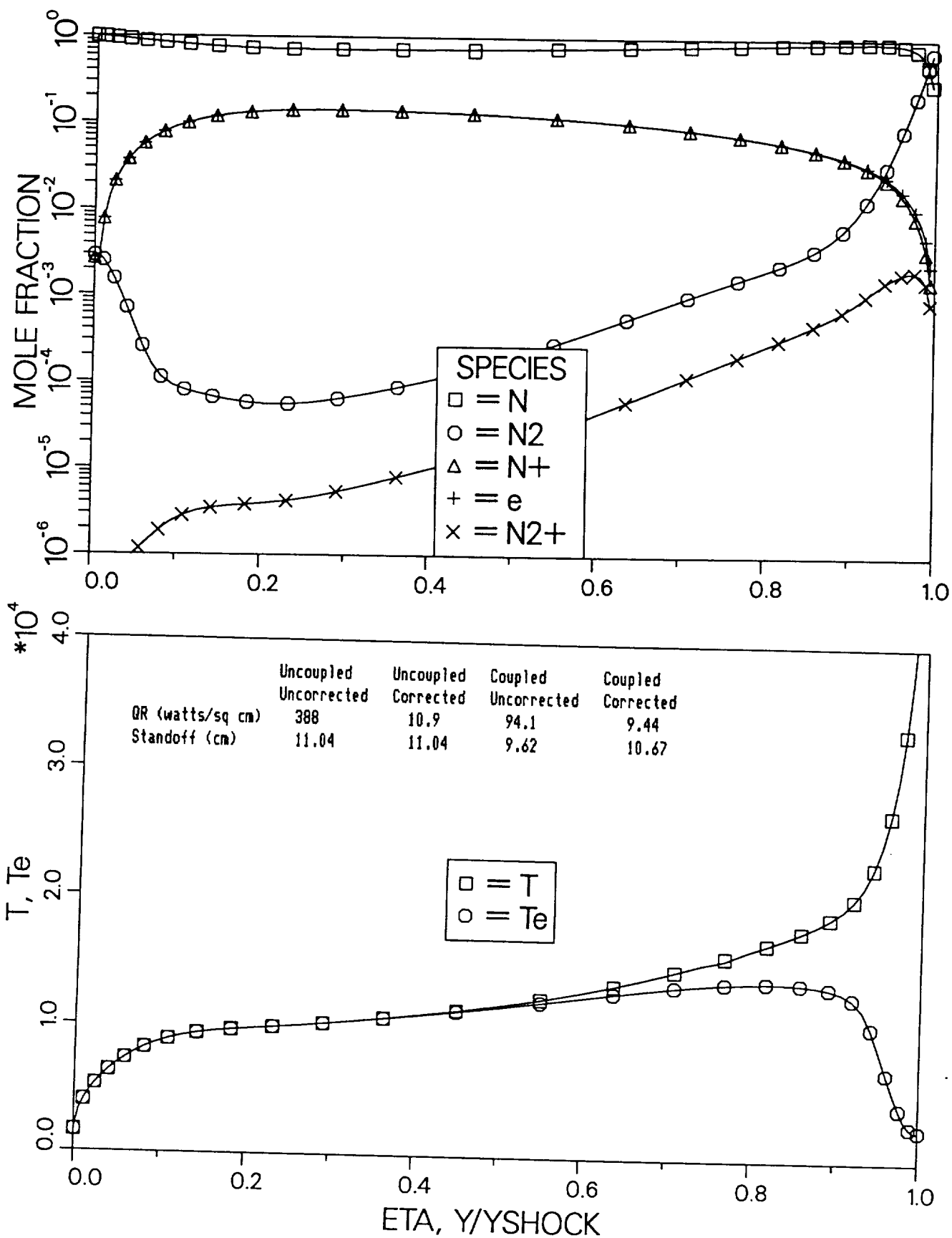


Fig. 8 -- Stagnation Profiles with Radiation Coupling and LTNE Effects
 $U = 12$ km/sec, $H = 80$ km, $R_{nose} = 2.3$ m
 $QR = 9.44$ watts/sq cm $\xi = 10.67$ cm

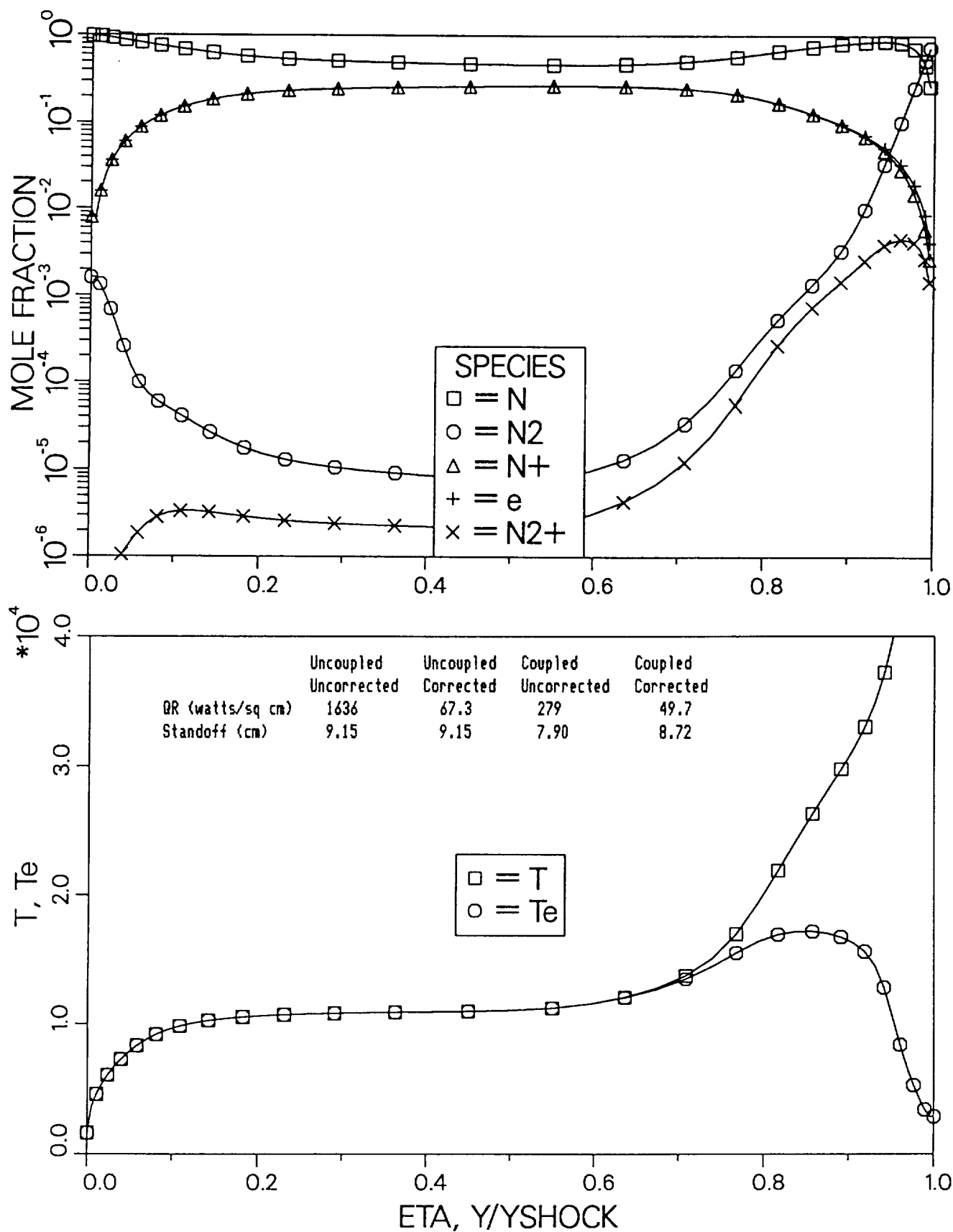


Fig. 9 -- Stagnation Profiles with Radiation Coupling and LTNE Effects
 $U = 14$ km/sec, $H = 80$ km, $R_{nose} = 2.3$ m
 $QR = 49.7$ watts/sq cm $\delta = 8.72$ cm

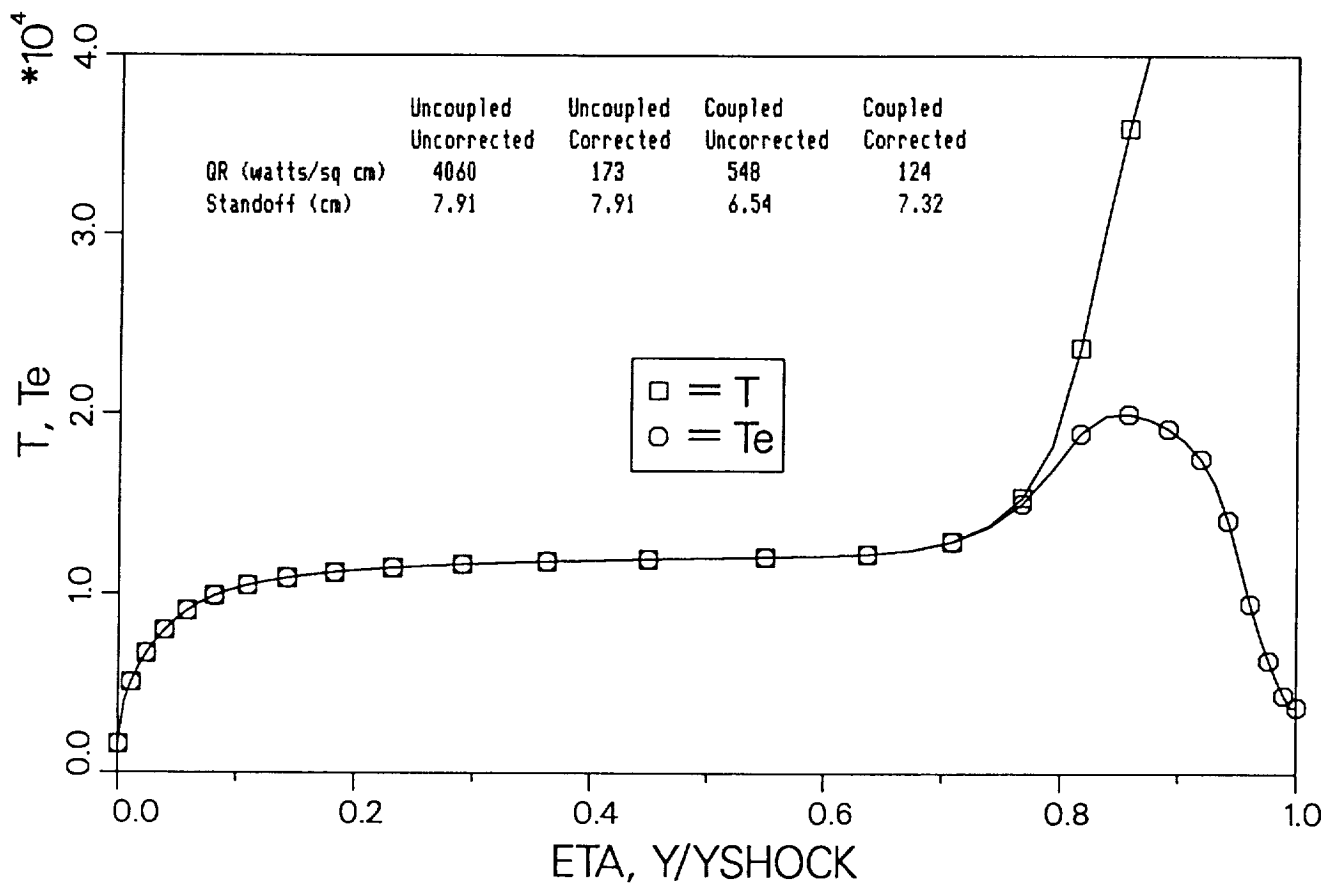
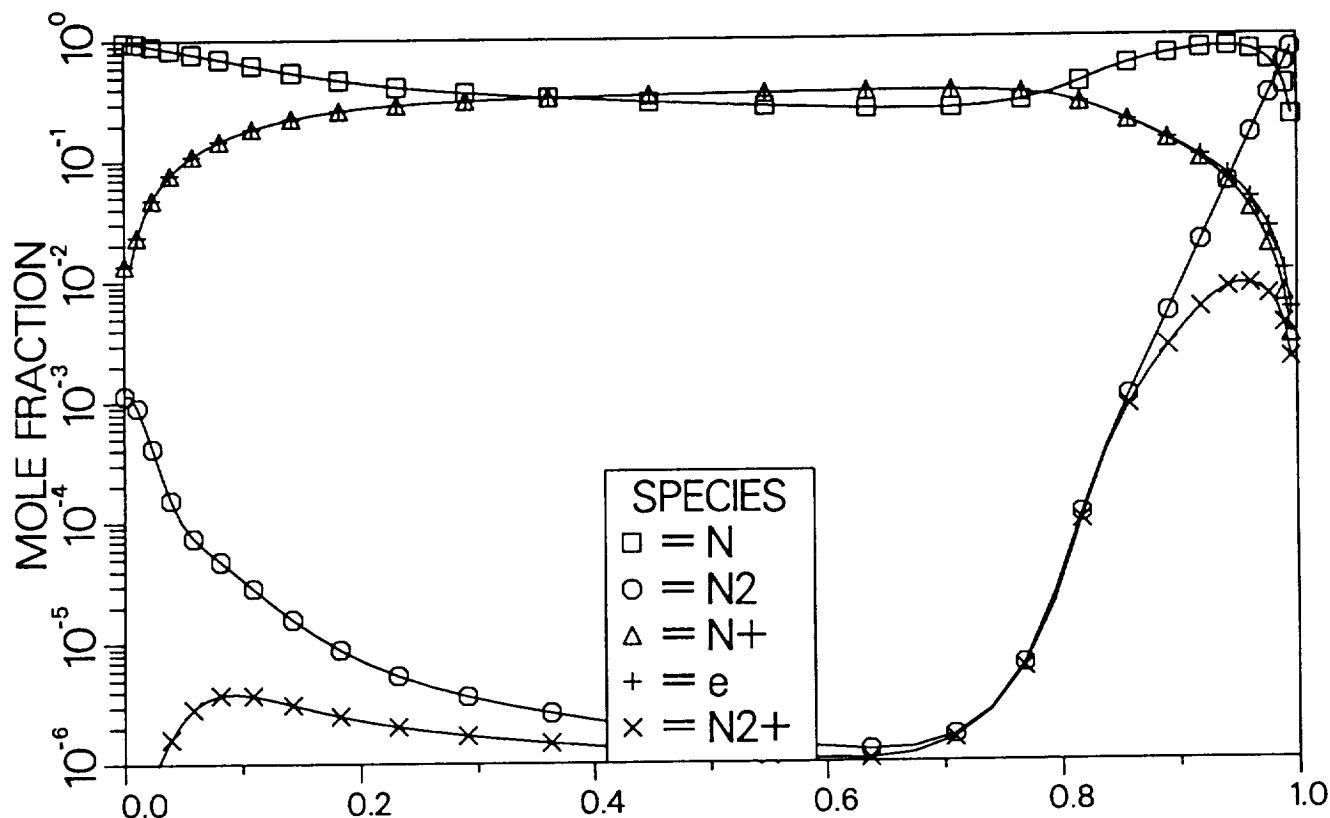


Fig. 10 -- Stagnation Profiles with Radiation Coupling and LTNE Effects
 U = 16 km/sec, H = 80 km, R_{nose} = 2.3 m
 QR = 124 watts/sq cm δ = 7.32 cm

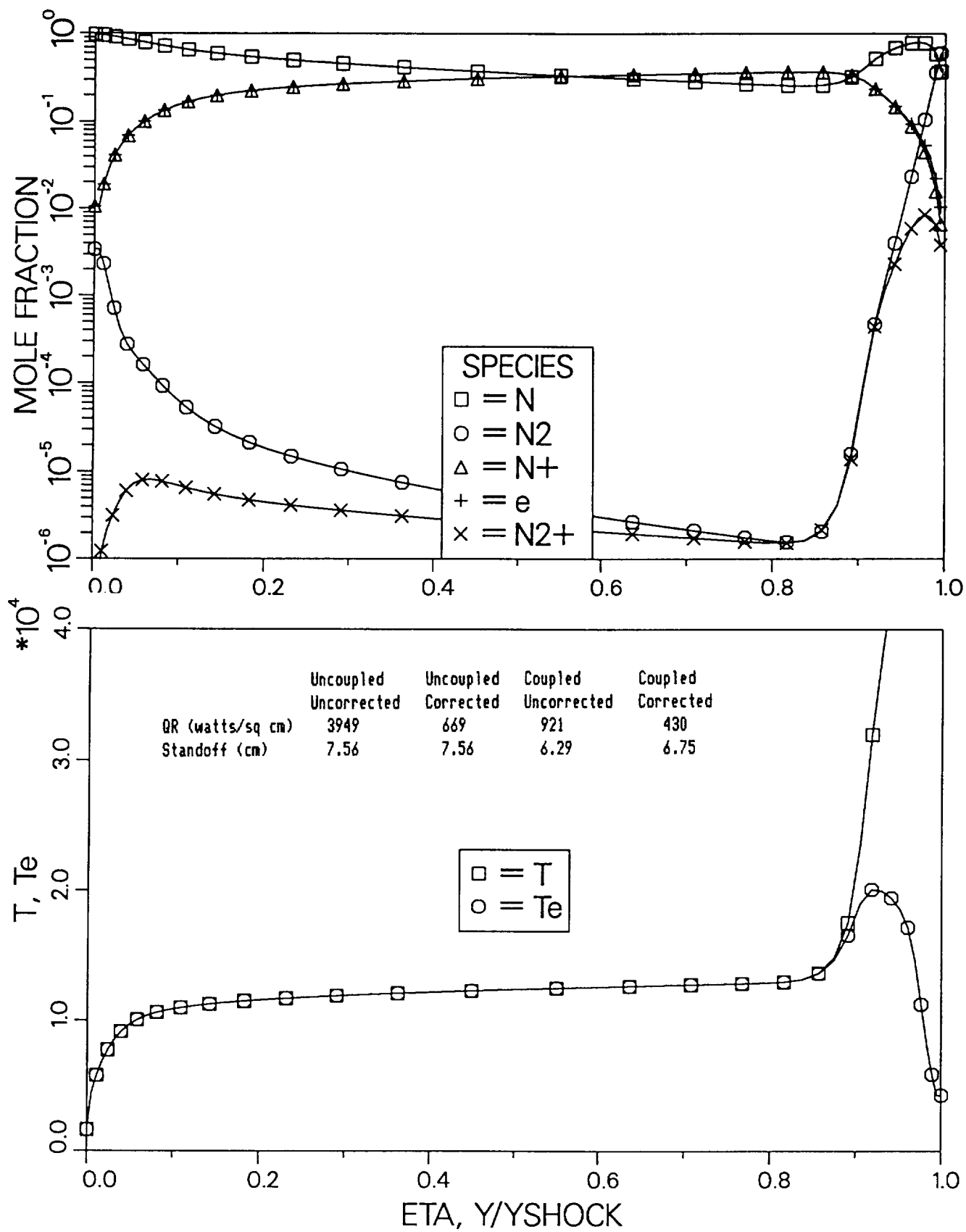


Fig. 11 -- Stagnation Profiles with Radiation Coupling and LTNE Effects
 $U = 16$ km/sec, $H = 75$ km, $R_{nose} = 2.3$ m
 $QR = 430$ watts/sq cm $\delta = 6.75$ cm

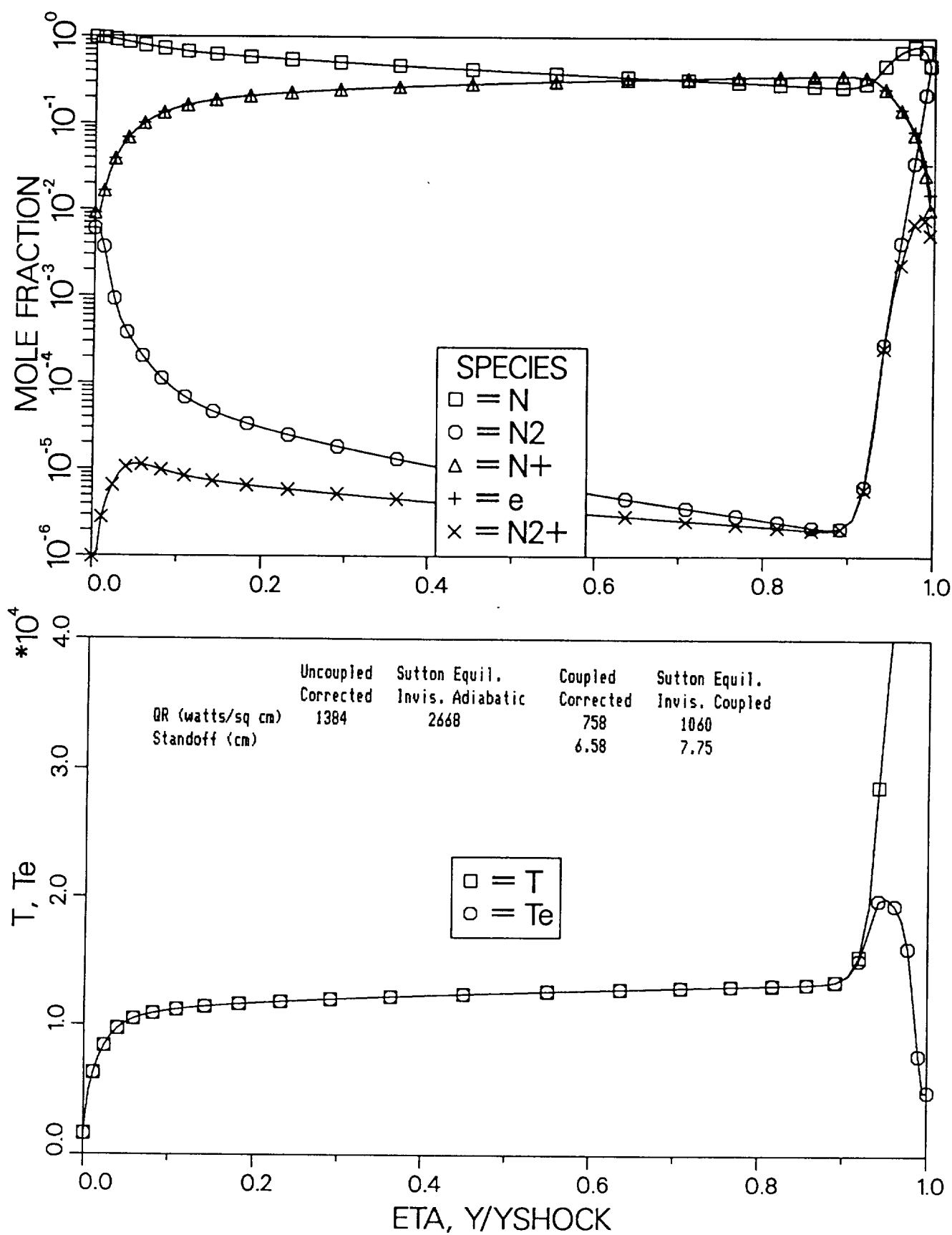


Fig. 12 -- Stagnation Profiles with Radiation Coupling and LTNE Effects
 $U = 16$ km/sec, $H = 72$ km, $R_{nose} = 2.3$ m
 $QR = 758$ watts/sq cm $\delta = 6.58$ cm

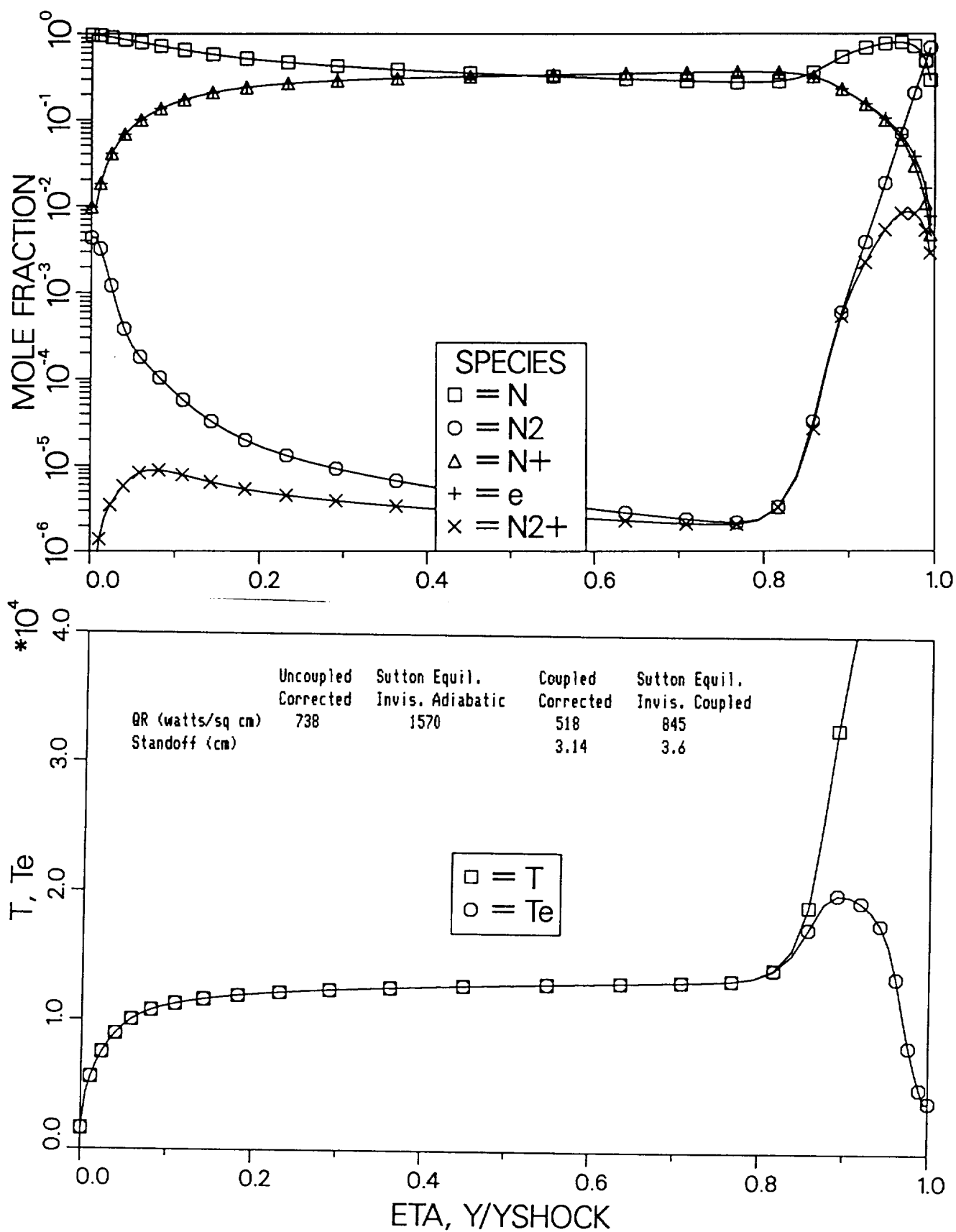


Fig. 13 -- Stagnation Profiles with Radiation Coupling and LTNE Effects
 $U = 16$ km/sec, $H = 72$ km, $R_{nose} = 1$ m
 $QR = 518$ watts/sq cm $\delta = 3.14$ cm

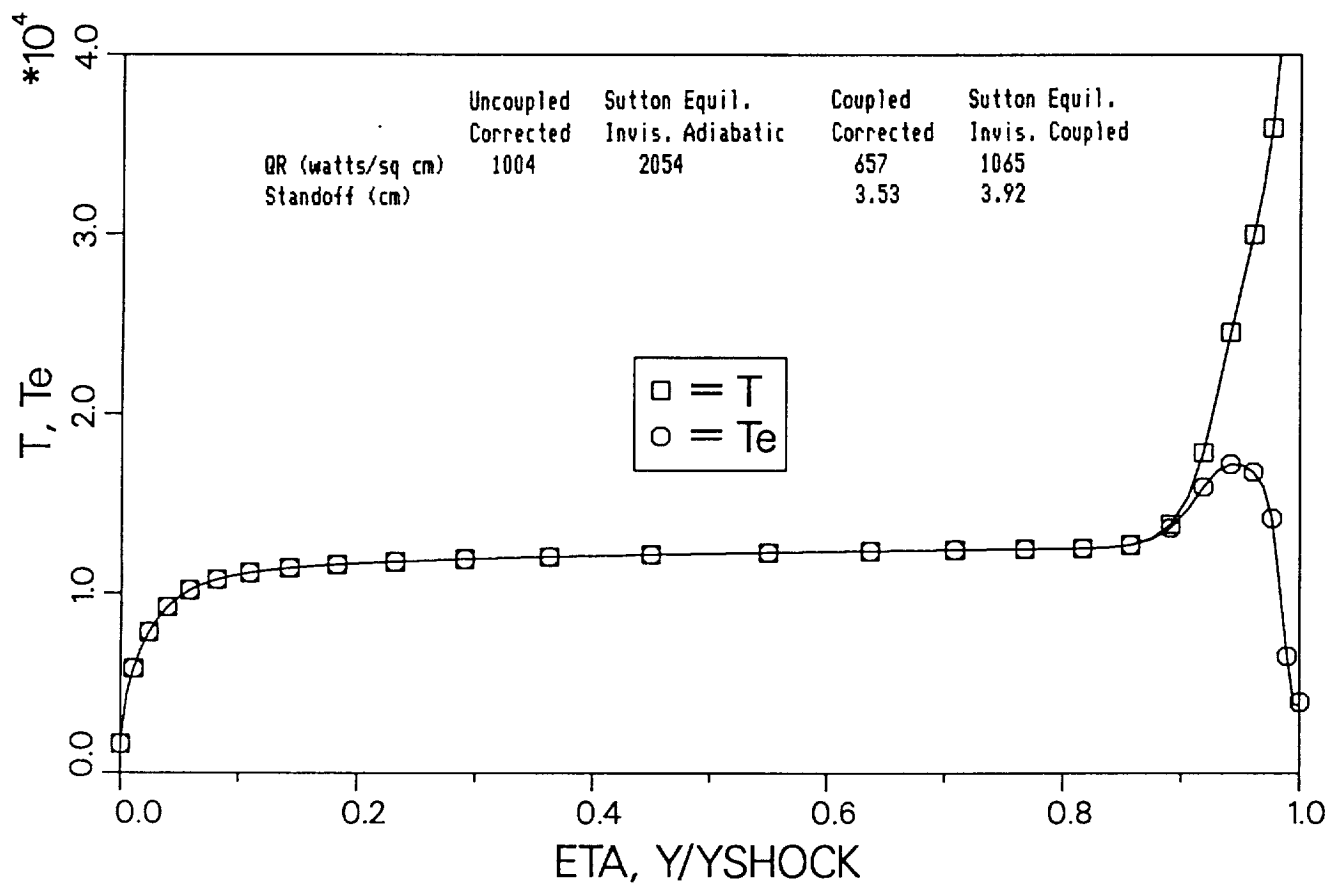
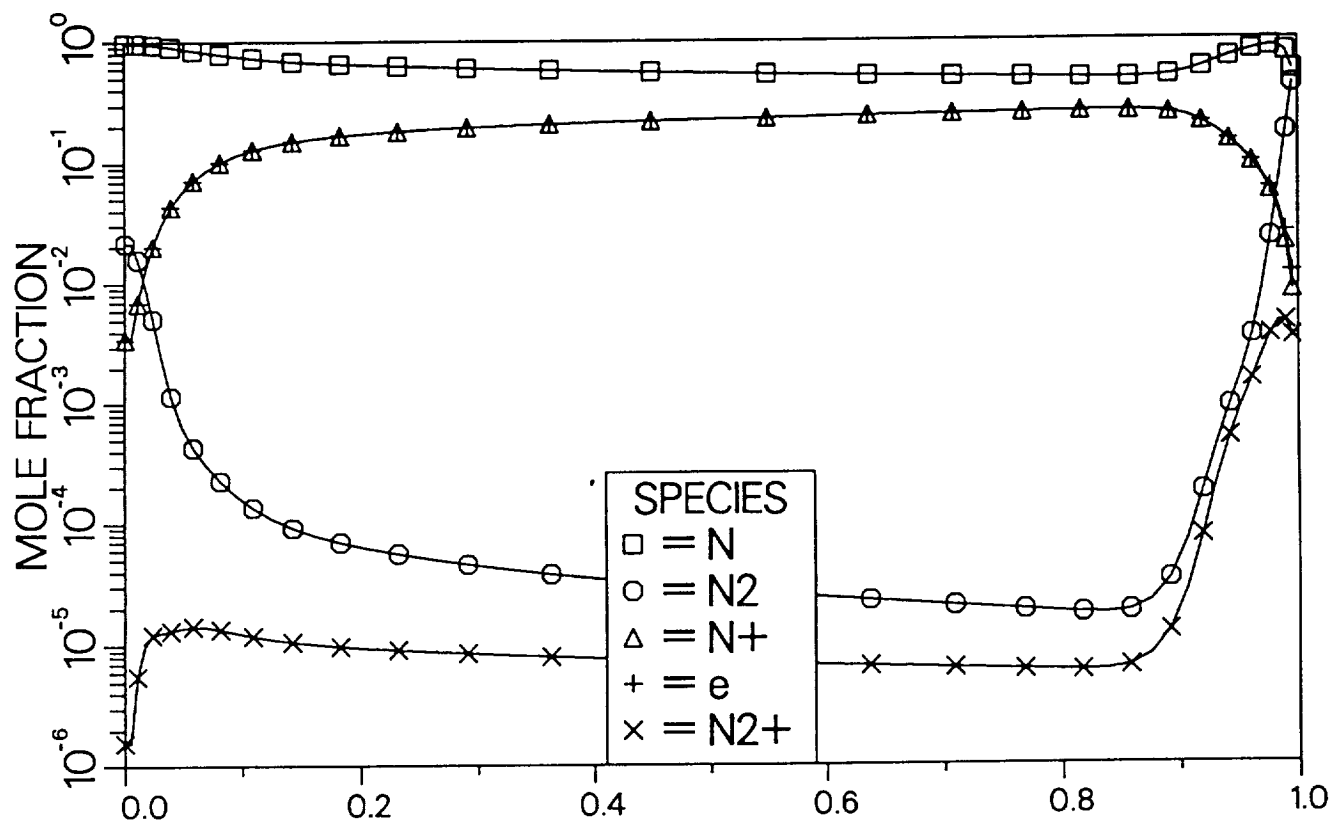


Fig. 14 -- Stagnation Profiles with Radiation Coupling and LTNE Effects

U = 14 km/sec, H = 66 km, R_{nose} = 1 m

QR = 657 watts/sq cm ζ = 3.53 cm

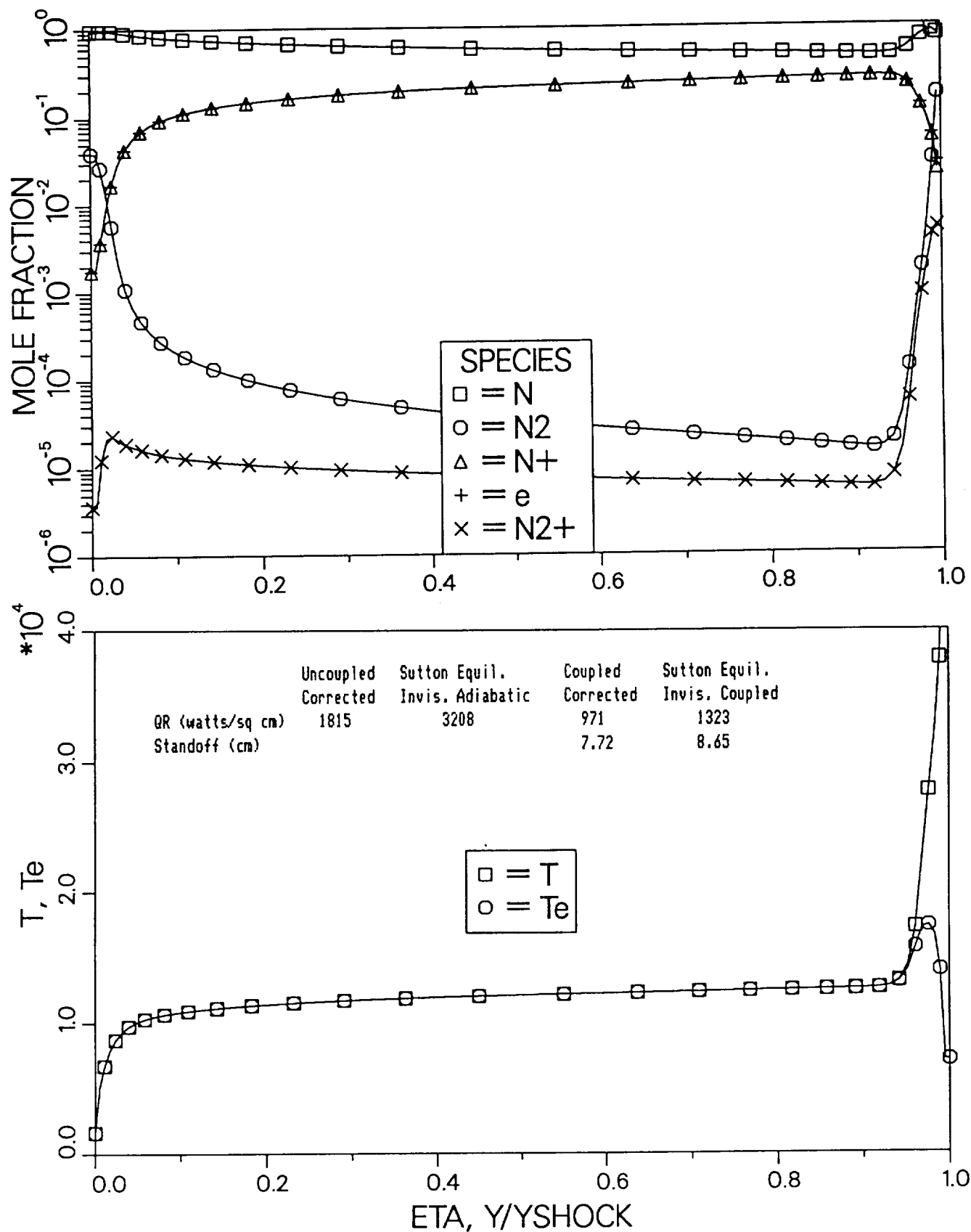


Fig. 15 -- Stagnation Profiles with Radiation Coupling and LTNE Effects
 $U = 14$ km/sec, $H = 66$ km, $R_{nose} = 2.3$ m
 $QR = 971$ watts/sq cm $\delta^* = 7.72$ cm

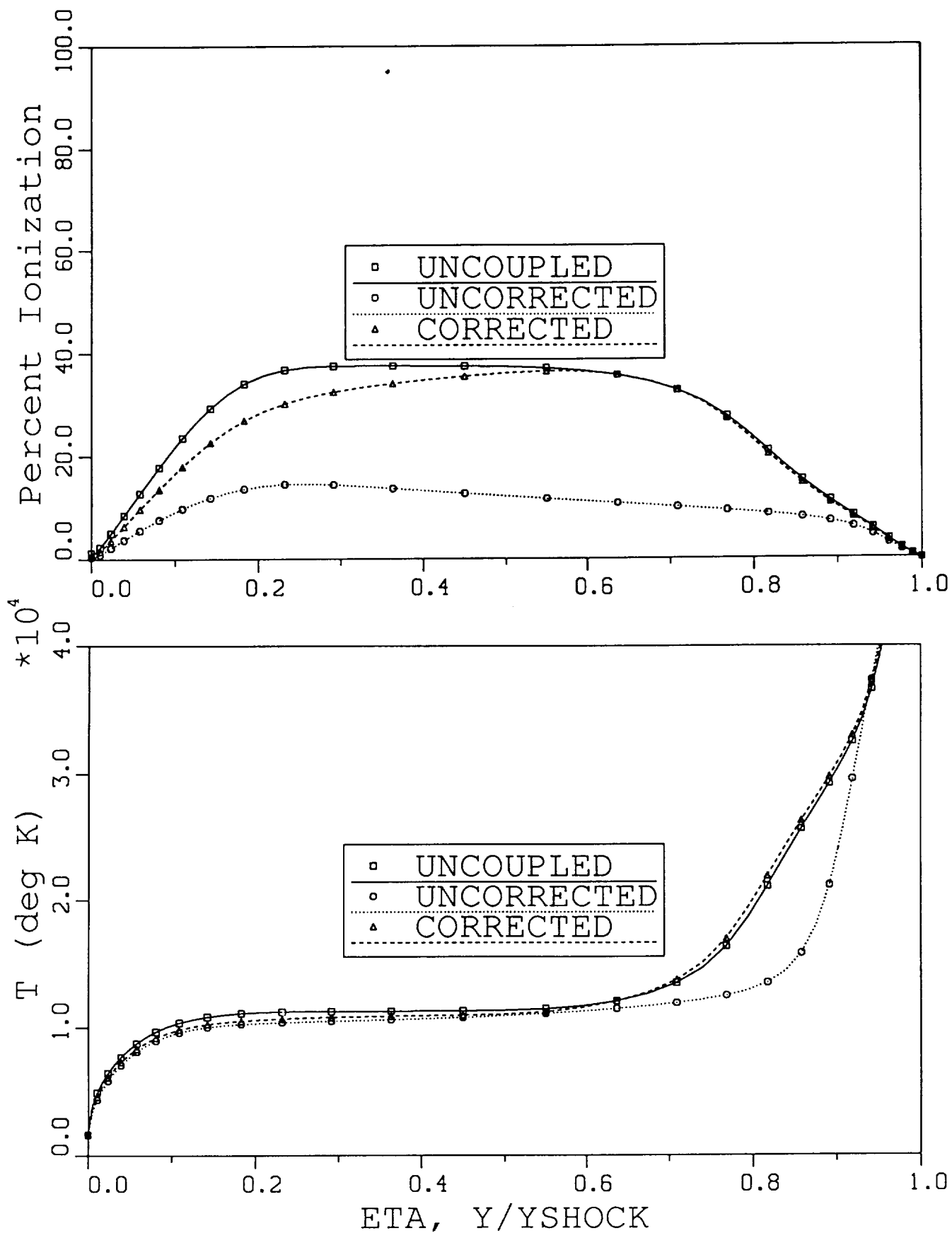


Fig. 16 -- Comparison of Uncoupled, Coupled Uncorrected, and Coupled Corrected Profiles
 $U = 14$ km/sec, $H = 80$ km, $R_{\text{nose}} = 2.3$ m
 (This figure is not specifically mentioned in the text.)

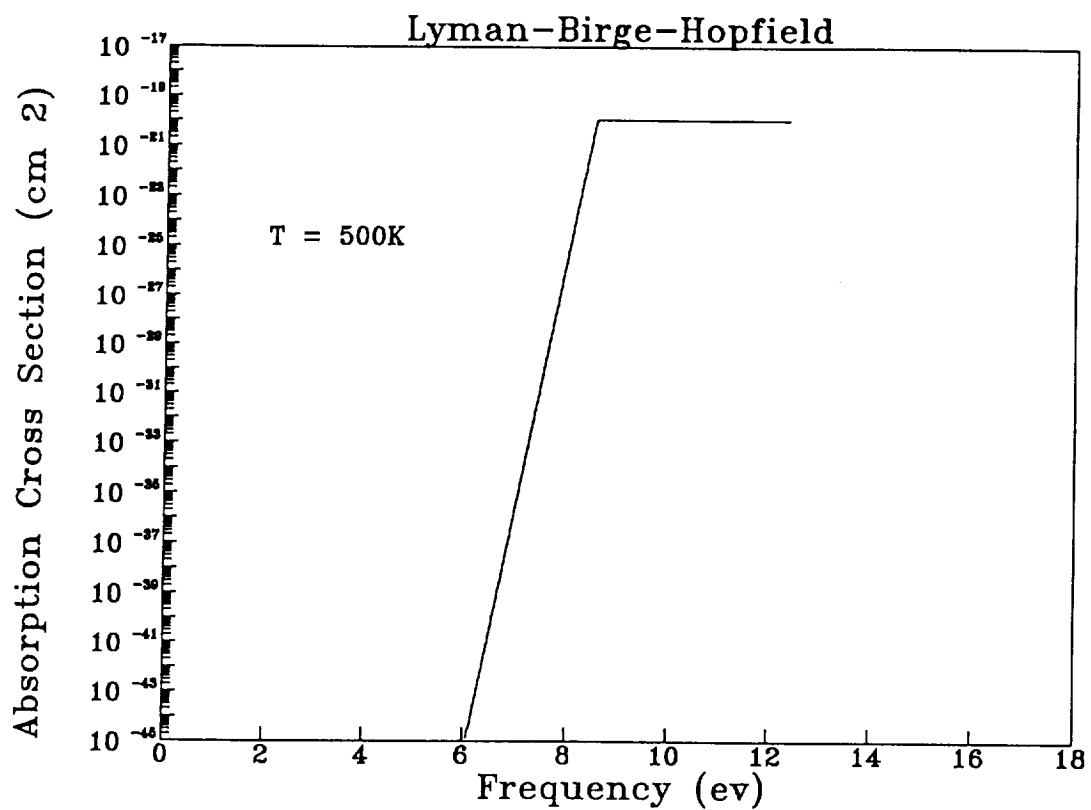


Fig. 17 -- Absorption Cross Section for Lyman-Birge-Hopfield Band
at T = 500 K

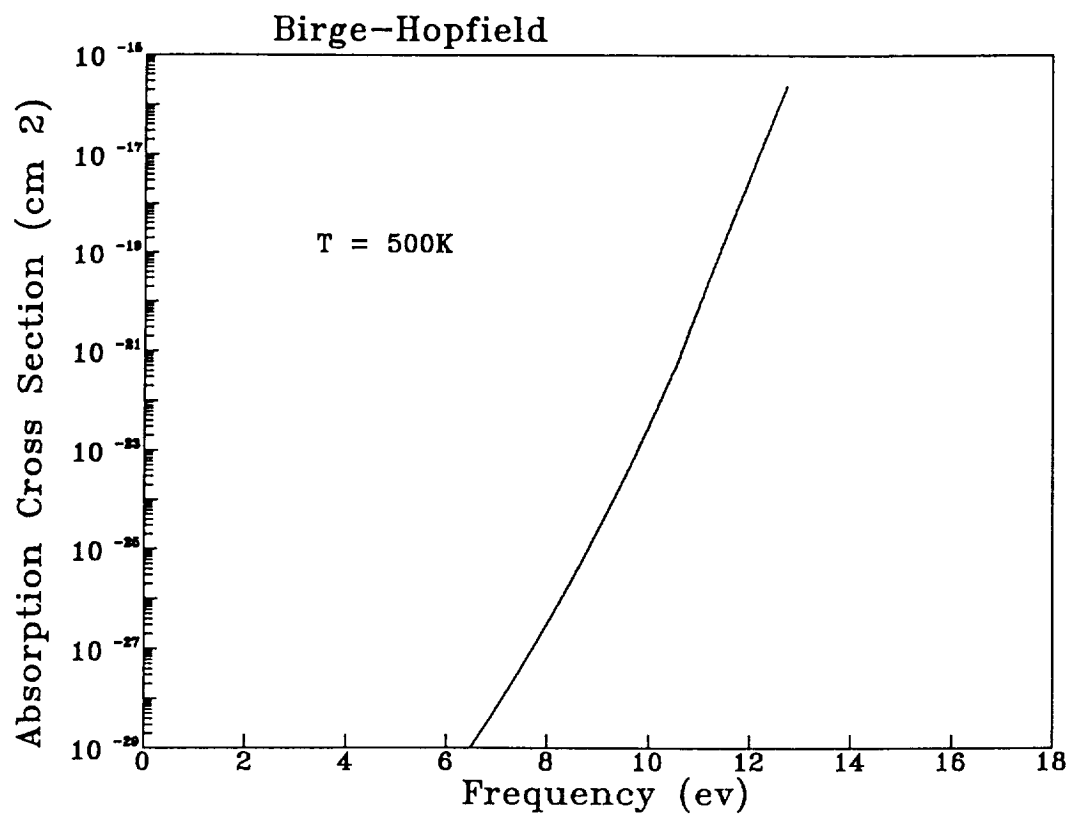


Fig. 18 -- Absorption Cross Section for Birge Hopfield Band
at $T = 500\text{ K}$

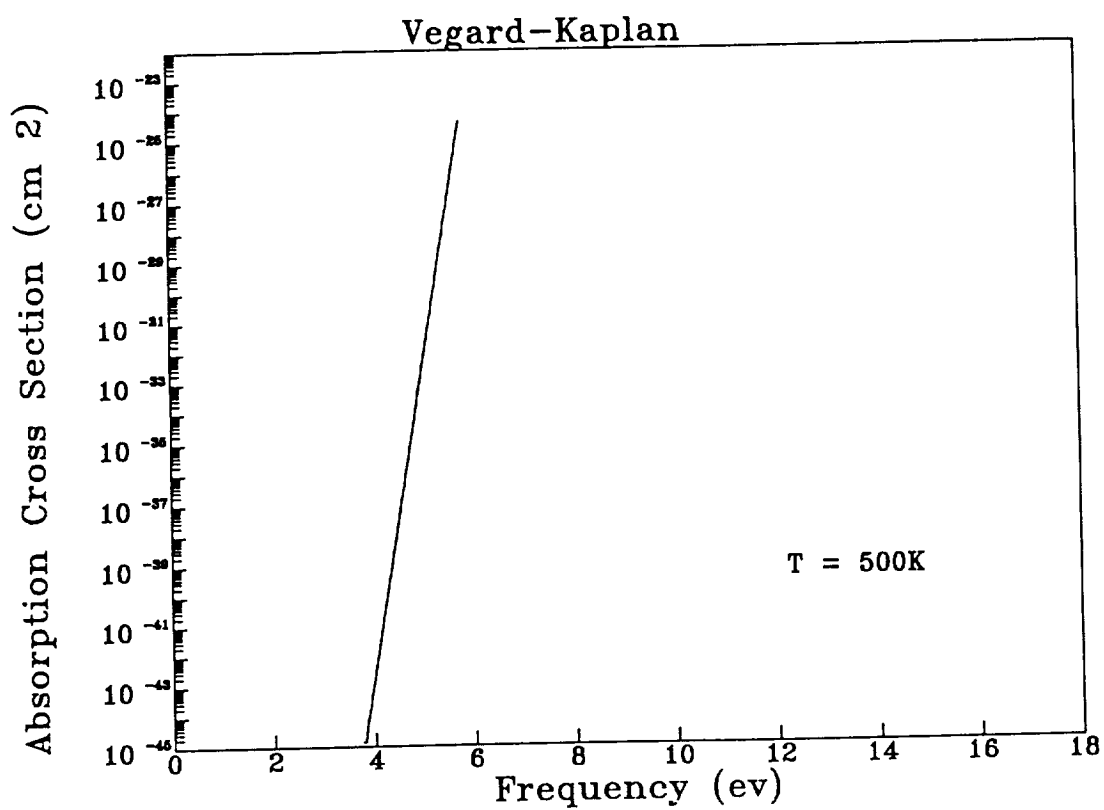


Fig. 19 -- Absorption Cross Section for Vegard-Kaplan Band
at T = 500 K

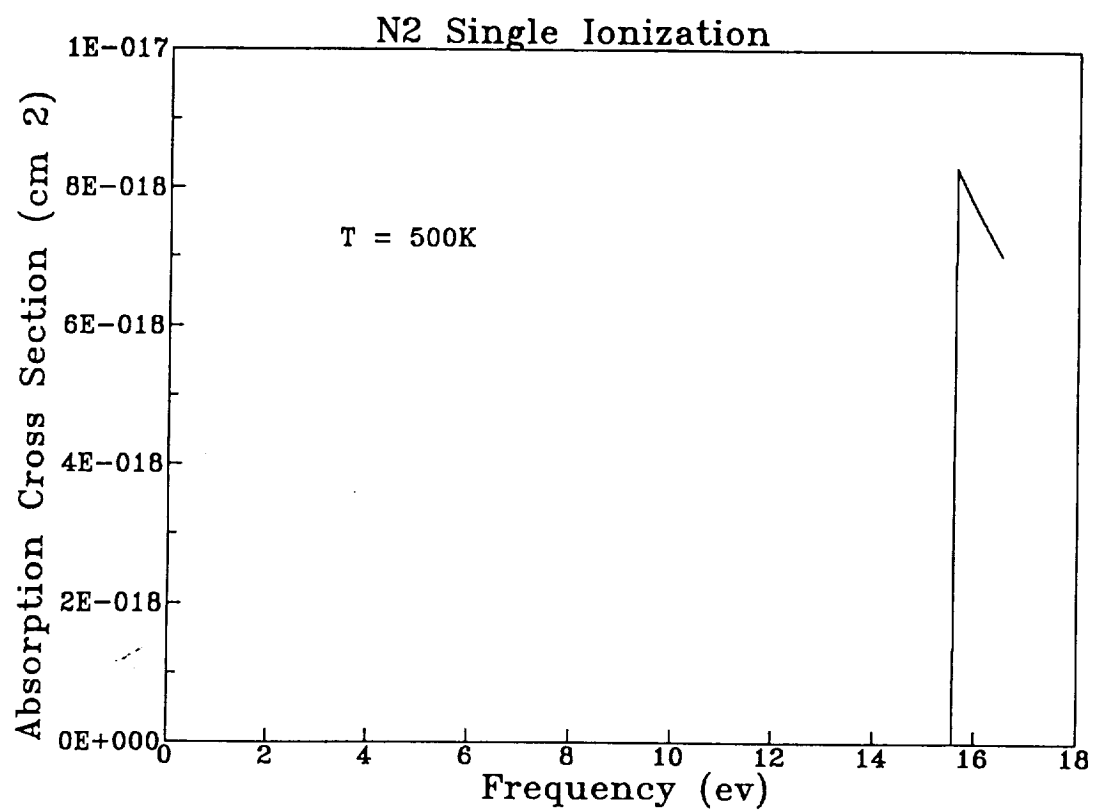


Fig. 20 -- Absorption Cross Section for N2 Single Ionization
at $T = 500 K$

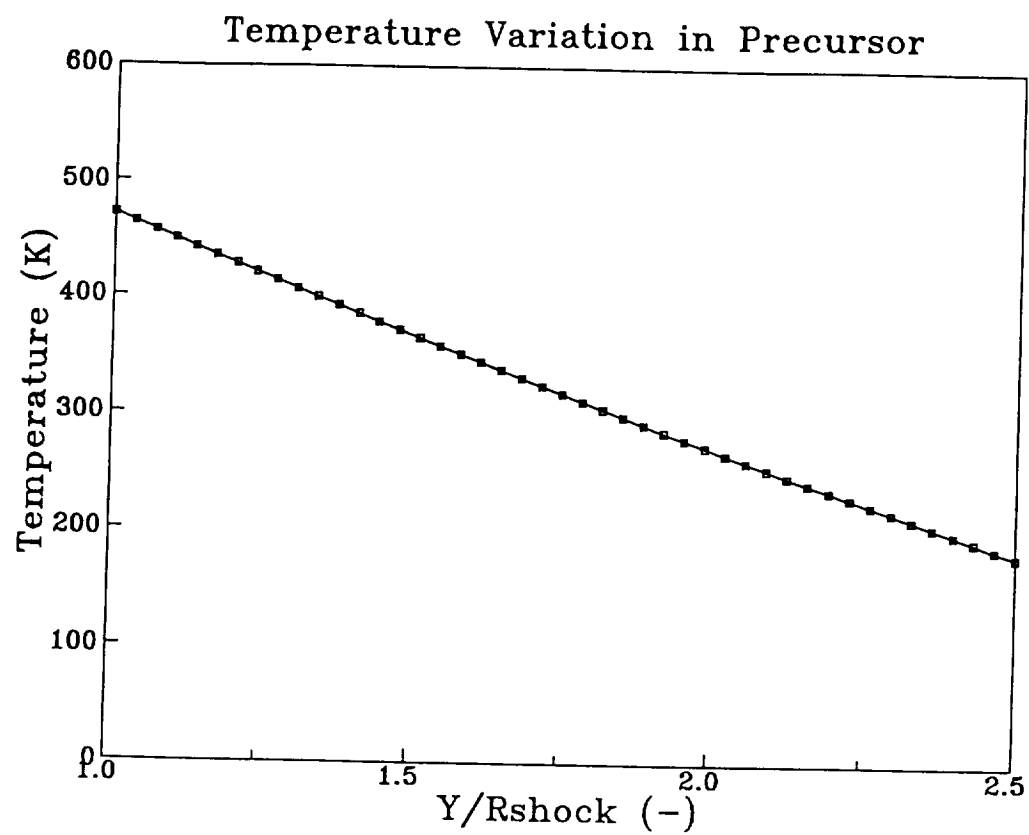


Fig. 21 -- Temperature Variation in the Precursor

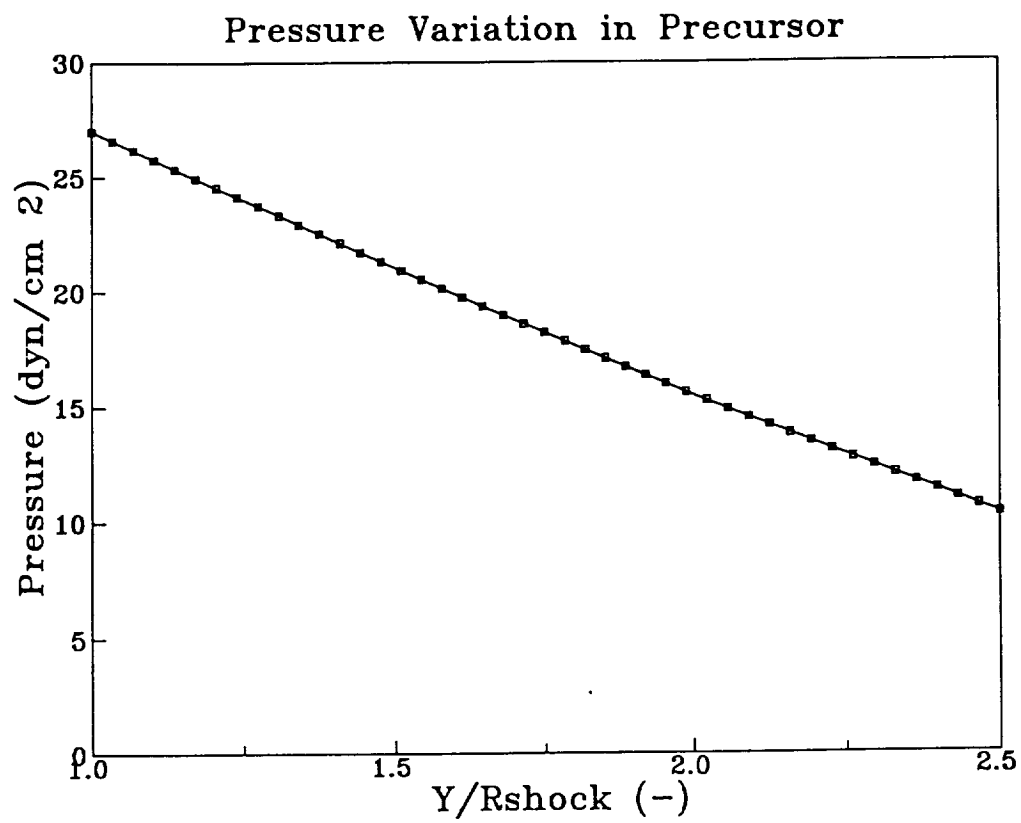


Fig. 22 -- Pressure Variation in the Precursor

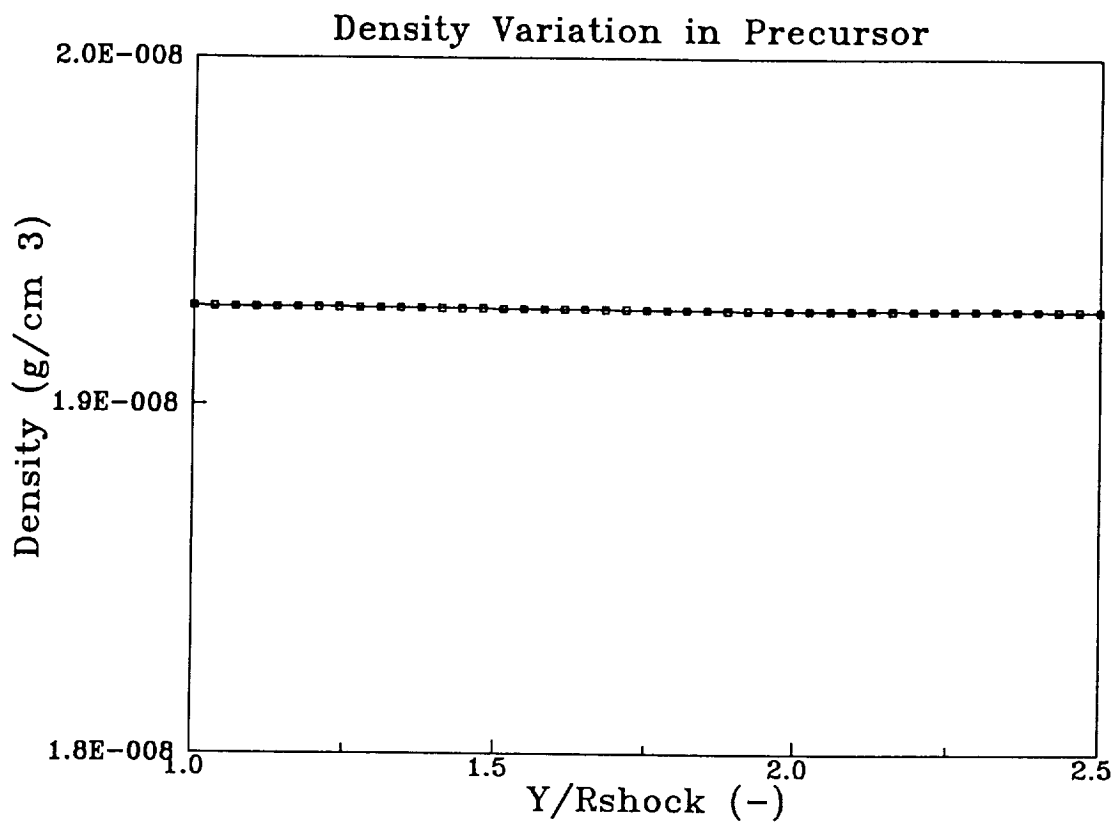


Fig. 23 -- Density Variation in the Precursor

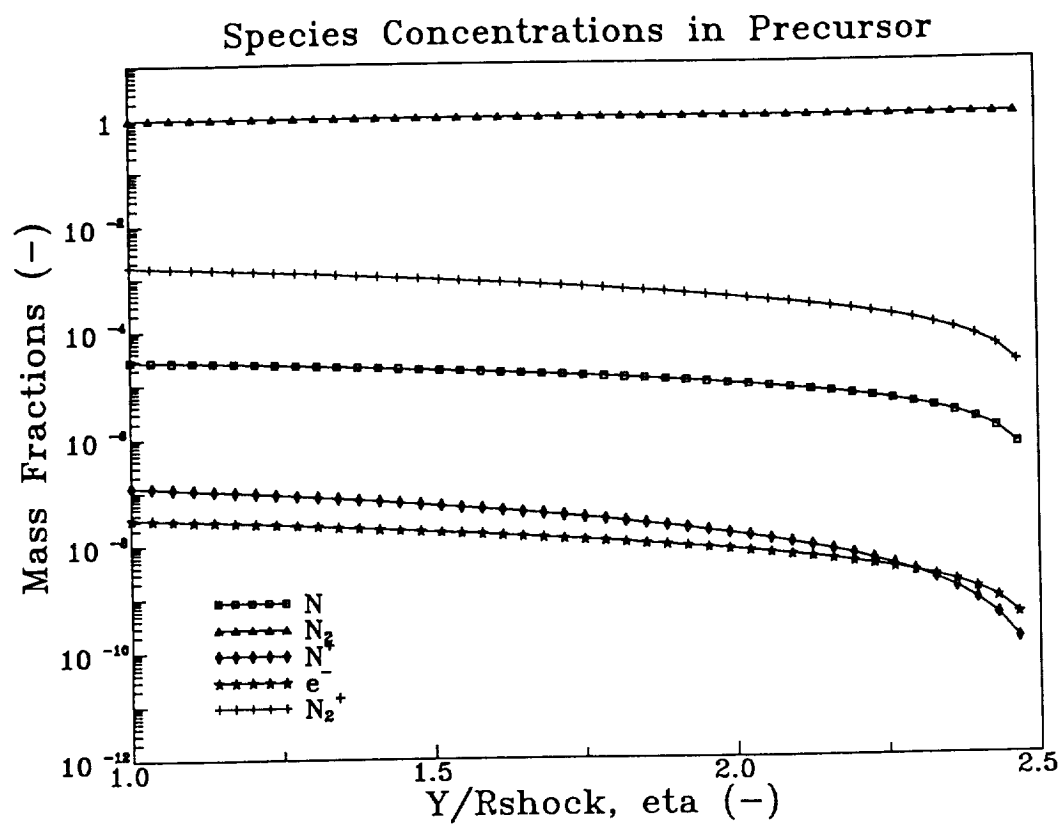


Fig. 24 -- Species Concentrations in the Precursor